POLITECNICO
MILANO 1863

Electronic dynamics of a topological insulator and a charge density wave compound studied with time-resolved ARPES

Candidate: **Flavien MUSEUR**   Supervisor: **Claudia Dallera**
Matricule: 894411

July 19, 2021

Summary

The electronic structure of a material plays a critical role in the determination of many of its macroscopic properties. Why some materials are transparent and some other opaque, why some conduct electricity and heat better than others, why some are magnetic, can all be understood by investigating how electrons in the material organize themselves, how they move and how they interact with the other degrees of freedom. Time and angle-resolved photoemission spectroscopy (TR-ARPES) is an experimental technique which has the capabilities of not only directly visualizing the band structure and Fermi surface, but also following their temporal evolution after excitation by an intense ultrafast laser pulse on a sub-picosecond scale. In this thesis, we will first present the general principles of the TR-ARPES technique as developed and used at the Physics Laboratory at the Politecnico di Milano. Then, it will be used to study the electronic dynamics of two quantum materials. The first one is a topological insulator, a type of material insulating in the bulk but conducting on the surface. The conduction and valence states have contrasted dynamics that will be evidenced using TR-ARPES. We will also track the opening of a gap caused by the deposition of magnetic impurities on the surface. The second material belongs to the so-called charge density waves (CDW) compounds, in which the electronic density becomes spontaneously non-uniform below a certain temperature. In our case this it is accompanied by a lattice distortion, corresponding to a new phonon. TR-ARPES can reveal the interplay between the electronic phase at low temperature and the CDW lattice mode. This work contributed to the publication of an article [1].

Sommario

La struttura elettronica di un materiale ha un ruolo fondamentale nella determinazione di molte delle sue proprietà macroscopiche. Perché alcuni materiali sono trasparenti e altri opachi, perché alcuni conducono elettricità e calore meglio di altri, perché alcuni sono magnetici, tutto può essere comrpeso studiando come si organizzano gli elettroni nel materiale, come si muovono e come interagiscono con gli altri gradi di libertà. La spettroscopia di fotoemissione risolta in tempo e angolo (TR-ARPES) è una tecnica sperimentale che ha la capacità non solo di visualizzare direttamente la struttura a bande e la superficie di Fermi, ma anche di seguirne l'evoluzione temporale dopo l'eccitazione da parte di un intenso impulso laser ultraveloce su una scala di sub-picosecondi. In questa tesi, presenteremo innanzitutto i principi generali della tecnica TR-ARPES sviluppata e utilizzata presso il Laboratorio di Fisica del Politecnico di Milano. Quindi, verrà utilizzato per studiare la dinamica elettronica di due materiali quantistici. Il primo è un isolante topologico, un tipo di materiale isolante nel volume ma conduttore in superficie. Gli stati di conduzione e di valenza hanno dinamiche contrastanti che verranno evidenziate utilizzando TR-ARPES. Ci occupiamo anche dell'apertura di una gap causata causata dalla deposizione di impurezze magnetiche sulla superficie. Il secondo materiale appartiene ai cosiddetti composti delle onde di densità di carica (CDW), in cui la densità elettronica diventa spontaneamente non uniforme al di sotto di una certa temperatura. Nel nostro caso questo è accompagnato da una distorsione del reticolo, corrispondente ad un nuovo fonone. TR-ARPES può rivelare l'interazione tra la fase elettronica a bassa temperatura e il modo CDW del reticolo. Questo lavoro ha contribuito alla pubblicazione di un articolo [1].

Contents

List of Figures

List of Figures

List of Figures

1 Time-resolved ARPES: general principles and experimental setup

1.1 Fundamentals of ARPES

1.1.1 The photoemission phenomenon

Photoemission is the process by which an electron inside a material is ejected after absorbing a photon of sufficient energy. In a first approximation, the process can be described using the conservation of energy: $E_{kin} = \hbar\omega - \phi - |E_b|$. E_{kin} is the kinetic energy of the ejected electron, ϕ is the work function of the material, and E_b is the binding energy, which is the energy difference between the state the electron was in before photoexcitation and the Fermi level of the material. The energy distribution of the emitted electrons thus contain information about the band structure of the material. In order to understand more precisely what the photoemission current depends on, one first needs to choose a model of the photoemission process. The mainstream approach is the phenomenological *three-step model* (figure 1.1.1 (b)), where the photoemission is divided in three independent steps [2]:

i . An electron in the solid is excited from an initial to a final bulk Bloch eigenstate by absorbing the incoming photon,

ii . The excited electron then travels to the sample surface

iii . Finally it escapes into vacuum after transmission through the surface potential barrier.

A complete description of this process must take into account not only the conservation of energy mentioned above, but also the conservation

Figure 1.1.1: (a) General geometry of an ARPES experiment. The emission direction of the photoelectron is specified by the polar (ϑ) and azimuthal (ϕ) angles. (b) and (c) Graphical representations of the three-step model (b) and the one-step model (c). Figure adapted from [2].

of momentum between the initial and the final states. The general geometrical configuration of an angle-resolved photoemission spectroscopy (ARPES) experiment is shown in panel (a) of figure 1.1.1.

Step (ii) of the three-step model can be modeled by a transport coefficient related to the inelastic mean free path of excited electrons in solids. This length is of the order of a few nanometers for electron energies of a few electronvolts. ARPES is thus fundamentally a surface sensitive technique. Step (iii) is described by a transmission probability through the interface with vacuum. It is found by matching the bulk Bloch eigenstates to free-electron plane waves in vacuum. The translation symmetry in the $x-y$ plane at the interface imposes the conservation of the parallel component of the electron momentum during the process. Moreover, the emitted photoelectron has a parabolic dispersion relation: $E_{kin} = \hbar^2 k^2 / 2m_e$. Therefore, we can simply link the in-plane electron momentum to its energy and emission angle:

$$k_{\parallel} = \frac{1}{\hbar} \sqrt{2 m_e E_{kin}} \cdot \sin(\vartheta) \qquad (1.1.1)$$

where ϑ is the polar angle defined in figure 1.1.1 (a). Given that E_{kin} cannot surpass $\hbar\omega - \phi$, this relation 1.1.1 shows that the size of the part of the Brillouin zone that we can probe is limited by the energy of the incoming photon. However, it is not as straightforward to find the value of the

perpendicular electron momentum, because it is changed at the transmission through the surface in a material-dependent way. This can be taken into account by defining for each material a parameter V_0, called the inner potential, such that:

$$k_\perp = \frac{1}{\hbar}\sqrt{2m_e(E_{kin}\cos(\vartheta)^2 + V_0)} \tag{1.1.2}$$

In this work, we will not focus on the determination of V_0. Consequently, only the $k_\parallel$ component will be considered.

1.1.2 Computation of the photoemission current

Step (i) of the three-step model is the most complex to describe, but it is the one that gives the most insight on the intrinsic electronic structure. The starting point is to find the probability to go from the initial state Ψ_i^N with N electrons to one final state Ψ_f^N, through optical excitation. This probability can be approximated by the Fermi golden rule [2]. The photoemission current is proportional to the sum of the transition probabilities for all possible initial and final states:

$$I(\mathbf{k}, E_{kin}) \propto \sum_{i,f} \left| \left\langle \Psi_f^N \middle| \hat{\mathbf{H}}_{int} \middle| \Psi_i^N \right\rangle \right|^2 \delta(E_f^N - E_i^N - \hbar\omega) \tag{1.1.3}$$

The Hamiltonian for the interaction with the photon can be written as $\hat{\mathbf{H}} = \frac{e}{m_e c}\mathbf{A}\cdot\hat{\mathbf{p}}$, by working in a gauge where the scalar potential Φ is zero, neglecting non-linear two-photon processes and assuming that the vector potential is uniform over atomic dimensions (this is the dipole approximation, which holds for UV photons). The energies can be readily separated into a photoelectron term and a $(N-1)$ electron term: $E_f^N = E_f^{N-1} + E_{kin}$ and $E_i^N = E_i^{N-1} - E_b(\mathbf{k})$. In order to simplify the expression of the transition probability, we would like to similarly factorize the wavefunctions Ψ_i^N and Ψ_f^N into a photoelectron wavefunction and a $(N-1)$ electron wavefunction. This is generally not possible, as the photoelectron will relax and interact with the system left behind; but it can be reasonably assumed for high kinetic-energy electrons, which are disturbed less by the scattering. We will therefore places ourselves within the *sudden approximation*, where the photoemission process is assumed to be sudden: the photoelectron decouples from the remaining system immediately after photoexcitation, before relaxation sets in. This approximation is extremely useful, as it gives the photoemission current a clear interpretation

in terms of intrinsic electronic properties. On the other hand, it will not reproduce the feature of the spectrum for low kinetic-energy electrons, which are more likely to suffer inelastic scattering events. This gives rise to an inelastic background which is usually ignored or subtracted. A more refined picture of the photoemission process is the *one-step model* (figure 1.1.1 (c)). This model directly considers the optical transition between initial and final states in terms of many-body wave functions that obey appropriate boundary conditions at the surface of the solid; but it is obviously much more complicated.

Within the sudden approximation, we may write [10]:

$$\Psi_f^N = \phi_{f,E_{kin}}^{\mathbf{k}} \sum_s \Psi_s^{N-1} \tag{1.1.4}$$

where $\phi_{f,E_{kin}}^{\mathbf{k}}$ is the wavefunction of the photoelectron with momentum $\mathbf{k}$ and kinetic energy E_{kin}, and Ψ_s^{N-1} are the excited states for $(N-1)$. Similarly,

$$\Psi_i^N = \phi_i^{\mathbf{k}} \Psi_i^{N-1} \tag{1.1.5}$$

where $\phi_i^{\mathbf{k}}$ is the wavefunction of the state from which the electron is emitted. With this factorization, we can rewrite the matrix elements of equation (1.1.3) as:

$$\left\langle \Psi_f^N \middle| \hat{\mathbf{H}}_{int} \middle| \Psi_i^N \right\rangle = \left\langle \phi_{f,E_{kin}}^{\mathbf{k}} \middle| \hat{\mathbf{H}}_{int} \middle| \phi_i^{\mathbf{k}} \right\rangle \cdot \sum_s \left\langle \Psi_s^{N-1} \middle| \Psi_i^{N-1} \right\rangle \tag{1.1.6}$$

The first term $\left\langle \phi_{f,E_{kin}}^{\mathbf{k}} \middle| \hat{\mathbf{H}}_{int} \middle| \phi_i^{\mathbf{k}} \right\rangle = M_{f,i}^{\mathbf{k}}$ is the one-electron dipole matrix element. The photoemission current is therefore proportional to:

$$I(\mathbf{k}, E_{kin}) \propto \sum_{i,f} \left| M_{f,i}^{\mathbf{k}} \right|^2 \cdot \sum_s \left| \left\langle \Psi_s^{N-1} \middle| \Psi_i^{N-1} \right\rangle \right|^2 \delta(E_{kin} + E_s^{N-1} - E_i^N - \hbar\omega) \tag{1.1.7}$$

The sum over s can be rewritten in a more understandable form, yielding the final expression for the photoemission current:

$$I(\mathbf{k}, E_{kin}) \propto A(\mathbf{k}, E_{kin} - \hbar\omega) f_{\text{FD}}(E_{kin} - \hbar\omega) \tag{1.1.8}$$

$f_{\text{FD}}(\omega)$ is the Fermi-Dirac distribution and signals that fact that this version of photoemission only probes the occupied electronic states. $A(\mathbf{k}, \omega)$ is the one-electron spectral function. It describes the probability with which an electron with energy ω and momentum $\mathbf{k}$ can be removed from

an electron system in its ground state. Equation (1.1.8) can be generalized out of equilibrium, with time-dependent spectral function and distribution functions [11]. But this approach is not valid when the pump overlaps with the probe. The rigorous non-equilibrium calculation of $I(\mathbf{k}, \omega, t)$ relies on the Keldysh formalism for non-equilibrium Green's functions and is outside the scope of this work [12].

1.1.3 Spectral function and Green's function

The one particle spectral function is linked to the retarded Green's function $G(\mathbf{k}, \omega)$ by the relation [2]:

$$A(\mathbf{k}, \omega) = \frac{-1}{\pi} \mathrm{Im}\left[G(\mathbf{k}, \omega)\right] \tag{1.1.9}$$

For the case of a non-interacting electron system, the retarded Green's function is given by:

$$G^0(\mathbf{k}, \omega) = \frac{1}{\hbar\omega - \varepsilon(\mathbf{k})}, \text{ so } A(\mathbf{k}, \omega) = \frac{1}{\pi}\delta(\hbar\omega - \varepsilon(\mathbf{k})) \tag{1.1.10}$$

So the spectral function is a perfectly sharp image of the non-interacting band structure. If we now switch on the interactions, the renormalization of the retarded Green's function is expressed in terms of the electron self-energy $\Sigma(\mathbf{k}, \omega)$:

$$G(\mathbf{k}, \omega) = \frac{1}{\hbar\omega - \varepsilon(\mathbf{k}) - \Sigma(\mathbf{k}, \omega)} \tag{1.1.11}$$

The spectral function becomes:

$$A(\mathbf{k}, \omega) = \frac{-1}{\pi} \frac{\mathrm{Im}\Sigma}{(\hbar\omega - \varepsilon(\mathbf{k}) - \mathrm{Re}\Sigma)^2 + \mathrm{Im}\Sigma^2} \tag{1.1.12}$$

The general effect of the interactions is to broaden the photoemission spectra, by turning the spectral function into a Lorentzian. The width of this Lorentzian is the imaginary part of the self-energy, which is directly linked to the lifetime of the quasi-particles: the broader the line shape, the smaller the life time of the quasi-particles excitations [10]. Therefore, we have shown that by measuring the photoemission current in an angle- and energy-resolved way, we can not only access the electronic band structure, but also probe many-body effects in solids.

1.2 Experimental setup

A setup for time- and angle-resolved photoemission spectroscopy must be able to produce intense ultrafast laser pulses for both the pump and the probe. A sketch of the optical setup used is shown in figure 1.2.1. It uses several high-end, non-linear optical components to generate a pump pulse at 1.82 eV (480 nm) and a probe pulse at 6.05 eV (205 nm) [3]. This probe energy only permits to probe a limited part of the Brillouin zone ($|k_\parallel| < 0.2$ Å^{-1}). In return, both the temporal and energy resolution are contained, at around 50 fs and 50 meV respectively. Indeed, as a result of the indeterminacy principle, it is not possible to improve the temporal and the energy resolutions at the same time without lowering the probe energy. The pump and the probe are then focused on the sample down to a spot size of about 100 micrometers. Space-charge broadening is a result
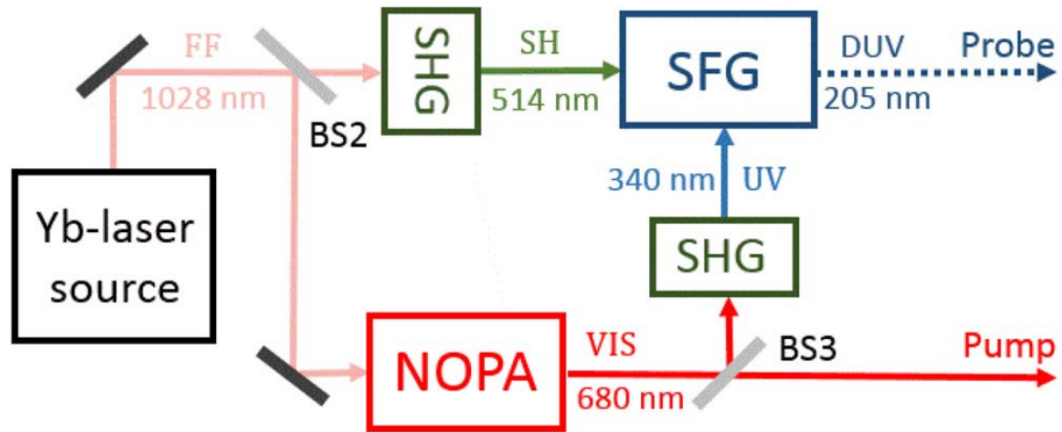
Figure 1.2.1: Simplified representation of the optical modules for the generation of pump and probe pulses. FF: fundamental frequency, SH: second harmonic, UV: ultraviolet, DUV: deep ultraviolet; SHG: second harmonic generation stage, NOPA: non- collinear parametric amplifier, SFG: sum-frequency generation stage, BS: beam-splitter. From [3].

of Coulomb repulsion among emitted photoelectrons, which broadens and shifts the spectra. Therefore, it is critical to keep the number of photoexcited electrons per pulse as low as possible; in our setup this is around 0.1 e^-/pulse. To keep the measurement time reasonable, the optical setup has a repetition rate of 100 kHz. The photoexcited electrons are sent into a hemispherical electron energy analyzer. This device disperses the electrons radially according to their energy using

an electric field. The electrons are then detected by a camera, with one axis of the sensor corresponding to the energy and the other to the photoemission angle. The aperture of the setup allows detection of photoexcited electrons in the range $\pm15°$.

The sample, as well as the part of the setup responsible for the detection of electrons are kept under ultra-high vacuum, with pressures of the order of 10^{-10} mbar. This is needed to detect the photoemitted electrons, as well as to preserve the sample surface quality. For this same reason, the samples can be cleaved *in situ* using a piece of carbon tape. Such a level of vacuum requires baking after every opening of the chamber, to remove all adsorbed atoms from the sides. The vacuum chamber is also equipped with other devices useful in surface science. One that we will use is the evaporator, which can deposit thin films on the sample by heating. Another relevant one is the low-energy electron diffraction (LEED) device, to check the crystalline orientation of the sample. Finally, it is possible to control the temperature of the sample inside the vacuum chamber. Cooling is done by pouring liquid nitrogen in the cryostat of the sample holder, and heating to 400 K can be achieved with resistors.

1.3 Analysis of TR-ARPES data

To analyse the data for this project, a Jupyter notebook was written in Python. The Jupyter software is particularly suited to an experimental data analysis workflow, thanks to the fact that the code is divided into cells that can be executed independently. This particular notebook is able to load the raw data from the camera, transform the angles of photoemission to $k_\parallel$ vectors according to equation (1.1.1), and makes it possible to explore the time-dependent data easily using interactive widgets. One of the main ways ARPES data are analyzed is through the study of energy curves (EDCs), which are the energy-dependent spectral weights at a fixed $k_\parallel$. These EDCs are then often fitted with various functions. As discussed in section 1.1.3, we expect the spectral function to experience a Lorentzian broadening caused by interactions. But this does not take into account the instrument resolution, which can be modeled by a Gaussian with a width of about 50 meV. Hence the ARPES data will almost always be fitted by the convolution of the Lorentzian spectral function with the Gaussian instrument resolution, which is called a Voigt function. The Voigt functions have no analytic expression, but they can be considered as contin-

uous interpolations between a Gaussian line shape and a Lorentzian line shape. Thus it can still be relevant to fit solely a simpler Lorentzian (Gaussian) function if the spectral feature of interest is really broad (narrow). In addition, if the zone of interest is close to the Fermi level, then the spectral line shape must be multiplied by the Fermi-Dirac distribution. If on the contrary the material has no clear feature at the Fermi level, one can put the material in electrical contact with a metal (often gold). The two materials will have the same Fermi level by definition, and this will be clearly visible on the ARPES signal of the metal. The Jupyter notebook created for this project enables the user to select EDCs at a given $k_{\parallel}$ for all delays, and define custom fit functions. All the ARPES figures in the following were produced with this code.

2 Capabilities of the system: study of a topological insulator

Topological insulators are new states of quantum matter that have attracted a lot of interests, both for their striking experimental properties and for the theoretical concepts used to describe them. This section will first present models of topological insulators, and then focus on experimental realizations of 3D topological insulators to demonstrate the capabilities of the TR-ARPES system.

2.1 Introduction to topological insulators

2.1.1 Quantum Hall effect and Chern insulators

The band theory of solids was one of the first achievements of quantum mechanics. It explains in simple terms how some crystals can conduct electricity and some others cannot, even though electrons are allowed to hop from an atom to another. Band insulators are materials with no partially filled bands: the set of valence bands is unambiguously separated from the set of conduction bands by an energy gap, which represents the energy cost to move an electron. In contrast, band conductors have partially filled bands, where there are plane wave states available for transport at arbitrarily low energy [13].

However, the discovery of the quantum Hall effect (QHE) in 1980 showed that this simple distinction does not give a complete picture of electronic transport in solids. Let us consider a slab of a metal in a perpendicular magnetic field, as shown on figure 2.1.1. From a classical point of view, the electrons in the bulk follow closed cyclotron-like trajectories. But on the edge of the sample, the orbits are opened as they repeatedly hit the edge. These skipping trajectories correspond to

the formation of edge states in a magnetic field. Note the unidirectional character of the edge trajectories: it is a direct consequence of the action of the Lorentz force on charge carriers. In a strong magnetic field, the
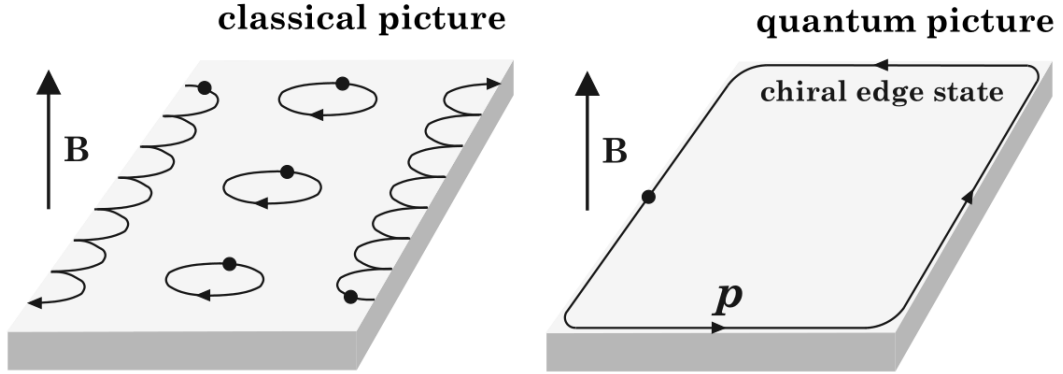
Figure 2.1.1: Classical and quantum picture of the Hall effect. From [4].

motion of the electron becomes quantized and the edge states form a one-dimensional channel on the boundary. To summarize, starting from the quantum Hall effect we have constructed a model of a material whose bulk is insulating but which has conductive edge states. In addition, the states in the edge channel are gapless and unidirectional, with their momentum locked to the magnetic field. This means that these states can conduct current without dissipation at low temperatures. Indeed, the main source of scattering in this regime is backscattering $\mathbf{k} \mapsto -\mathbf{k}$ caused by disorder in the electrostatic background; but such a process is forbidden, as there is no counter-propagating edge state. This robust directiveness is called *chirality*. As we will now see, it is a consequence of the breaking of the time reversal symmetry.

The *time reversal operation* $\mathscr{T}$ simply reverses the direction of the time arrow in a model: $t \mapsto -t$. Its effect on the most relevant quantum operators for an electron is the following:

$$\mathscr{T} \hat{\mathbf{r}} \mathscr{T}^{-1} = \hat{\mathbf{r}}$$
$$\mathscr{T} \hat{\mathbf{p}} \mathscr{T}^{-1} = -\hat{\mathbf{p}}$$
$$\mathscr{T} \hat{\sigma} \mathscr{T}^{-1} = -\hat{\sigma}$$

where σ is the vector of Pauli matrices. From the first two relations, one concludes that the canonical commutator $[\hat{\mathbf{r}}, \hat{\mathbf{p}}] = i\hbar$ is only conserved if $\mathscr{T} i \mathscr{T}^{-1} = -i$, meaning that $\mathscr{T}$ is antiunitary [14]. For a single electron, it
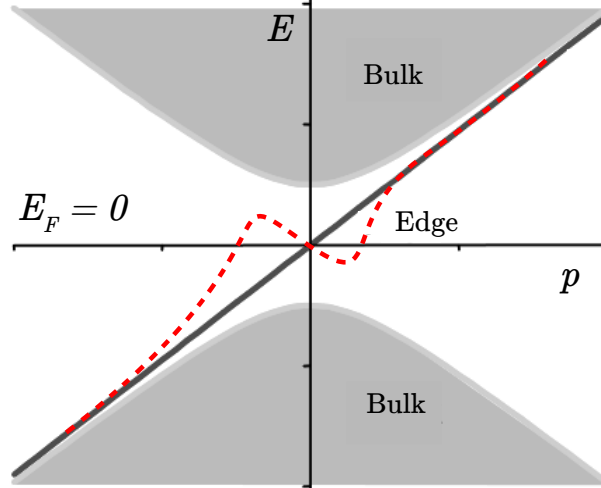
Figure 2.1.2: Black line: Chiral edge mode of the Chern insulator. Red dashes: modified edge mode with additional crossings of the Fermi level. Adapted from [4].

can be shown to have the property

$$\mathcal{T}^2 = -1 \Longleftrightarrow \mathcal{T}^{-1} = -\mathcal{T} \tag{2.1.1}$$

Finally, a system is said to be time reversal symmetric (TRS) if its Hamiltonian commutes with the time reversal operator:

$$\mathcal{T}\,\hat{\mathcal{H}}\,\mathcal{T}^{-1} = \hat{\mathcal{H}} \Longleftrightarrow \mathcal{T}\,\hat{\mathcal{H}} = \hat{\mathcal{H}}\,\mathcal{T} \tag{2.1.2}$$

This makes it possible to prove an important statement regarding a TRS single electron Hamiltonian. Consider an eigenstate $|+\rangle$ of a TRS Hamiltonian. Given the symmetry, the time reversed state $|-\rangle = \mathcal{T}\,|+\rangle$ is also an eigenstate at the same energy. Let us show that these two states are also orthogonal:

$$\langle +|-\rangle = \langle -|\,\mathcal{T}^\dagger \mathcal{T}^{-1}\,|+\rangle = -\langle -|\,\mathcal{T}^\dagger \mathcal{T}\,|+\rangle = -\langle -|+\rangle^* = -\langle +|-\rangle = 0 \tag{2.1.3}$$

This result, called *Kramers' theorem*, shows that any eigenstate of a TRS Hamiltonian is at least double degenerate [4]; for half-integer spin particles, it corresponds simply to the degeneracy between up and down spin states. This theorem gives more insight on the origin of the dissipationless edge state in the quantum Hall effect described above. Indeed, the application of an external magnetic field breaks the TRS, as it adds to a

free particle Hamiltonian terms like $\hat{\mathbf{A}} \cdot \hat{\mathbf{p}}$, $\hat{\mathbf{p}} \cdot \hat{\mathbf{A}}$ or $\hat{\sigma} \cdot \hat{\mathbf{B}}$ which are odd under time reversal. This allows the existence of edge states without a Kramers doublet, which would be available for backscattering.

This leaves the question of where in this model topology plays a role. It turns out that it is possible to break the TRS in a more general way, without any net magnetic flux [15]. This way, one can define an infinite set of TRS-breaking Hamiltonians which are related by a continuous change in their parameters. Although these Hamiltonians all have the same symmetry, they do not all correspond to the same phase of matter. The phase diagram is composed of several insulating phases, which differ by the value of an integer called a *topological invariant*. This number can have several definitions depending on the model considered. In the case of the quantum Hall effect, it is called the *(first) Chern number* and corresponds to the winding number of the phase of the electronic wave function on a path around the center of the Brillouin zone. A non-trivial (different from 0) value indicates that the phase cannot be defined continuously on the Brillouin zone, here because of broken time reversal symmetry.

The meaning of "topology" in this context can be further precised by a geometrical analogy. It is well known that two manifolds of the same genus can be deformed continuously into each other without creating holes. In the same way, insulating Hamiltonians can be adiabatically deformed [13], in the sense that:

- their parameters are changed continuously,

- they keep the same symmetries,

- the bulk gap remains open.

Then, two Hamiltonians with the same topological invariant can be adiabatically transformed into each other without a closure of the gap, which would indicate a quantum phase transition. This paradigm provides the most general explanation for the origin of the gapless edge states. At the interface between a topological insulator and the topologically trivial vacuum, the value of the topological invariant has to change from a non zero value to zero. This cannot be done without closing the gap, and thus guarantees the presence of gapless edge states with all topological insulators.

However, adiabatically equivalent Hamiltonians could have a different number of edge states. One could change the Hamiltonian close to the surface so that the edge state crosses the Fermi level more than one time.

For instance on figure 2.1.2, there are two edge modes of positive group velocity and one of negative group velocity. But the difference $N_R - N_L$ between the number of right and left moving modes cannot change, and is determined by the topological properties of the two systems in contact. For the Chern insulator, we have [5]:

$$N_R - N_L = \delta n \qquad (2.1.4)$$

where δn is the difference in the Chern number across the interface. Thus the topological invariant can be computed much more easily by looking at the number of edge states. This is the simplest example of *bulk-boundary correspondance*, a hallmark principle in topological insulators physics.

2.1.2 Quantum spin hall effect

We have seen that the interesting characteristic of Chern insulators require the breaking of time reversal symmetry, which is usually realized experimentally by applying an external magnetic field. But this prevents the use of powerful experimental techniques, specifically ARPES. Therefore, we now investigate whether time reversal symmetric topological insulators can exist.

A simple way to create a TRS system starting from the quantum Hall effect is to stack two copies of the Chern insulator on top of each other, with an effective magnetic field that acts in opposite ways for up and down spin species. Formally, this is done by doing the tensor product of the QHE Hilbert space with a two-state Hilbert space ($|1\rangle, |2\rangle$) corresponding to the two layers [13]. One layer will have its dynamics controlled by the original QHE Hamiltonian $\hat{\mathcal{H}}_{QHE}$, and the other by the time reversed conjugate $\mathcal{T} \hat{\mathcal{H}}_{QHE} \mathcal{T}^{-1}$. Thus, the total Hamiltonian reads

$$\hat{\mathcal{H}}_{tot} = |1\rangle \langle 1| \otimes \hat{\mathcal{H}}_{QHE} + |2\rangle \langle 2| \otimes \mathcal{T} \hat{\mathcal{H}}_{QHE} \mathcal{T}^{-1} \qquad (2.1.5)$$

By making use of the property 2.1.1 and renumbering the layers, one can see that this Hamiltonian is indeed time reversal symmetric. The construction is represented in figure 2.1.3.

In real materials, this concept can be realized through intrinsic *spin-orbit coupling*, where each layer represents a spin polarization of electrons. This interaction can be difficult to model in a tight-binding Hamiltonian, but its symmetry properties can be understood with the form used in atomic physics: $\hat{\mathbf{L}} \cdot \hat{\sigma}$, where $\hat{\mathbf{L}}$ is the orbital angular momentum. This shows that this coupling has the properties we are looking for:
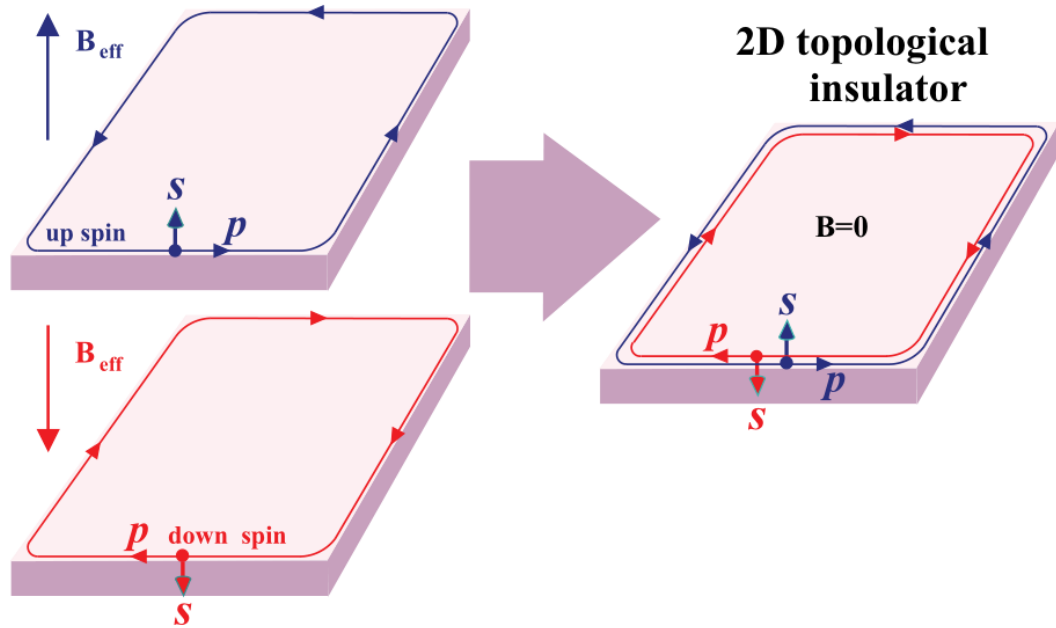
Figure 2.1.3: Quantum spin Hall effect an helicity on a 2D topological insulator. From [4].

- it is time-reversal symmetric,

- it acts in opposite ways on up and down spin electrons.

The consequence of introducing such an interaction is that the edge state of the QHE now forms a Kramers doublet: at each energy, there are two eigenstates related by the time reversal operation. These edge states also have a peculiar spin texture, called *helicity*, characterized by the locking between the spin and momentum direction. As shown on figure 2.1.3, right-moving edge electrons must have a spin up, whereas left-moving electrons have a spin down. In consequence, the topological protection is slightly weaker than in the case of the QHE. Backscattering processes between the edge modes are allowed, but only if they are able to flip the spin of the electron. In other words, the edge states are *protected by the time reversal symmetry*, given that a disorder potential with such a symmetry cannot flip an electron spin. To prove this, let us consider again two edge states $|\pm\rangle$ forming a Kramers doublet, and a TRS scattering potential
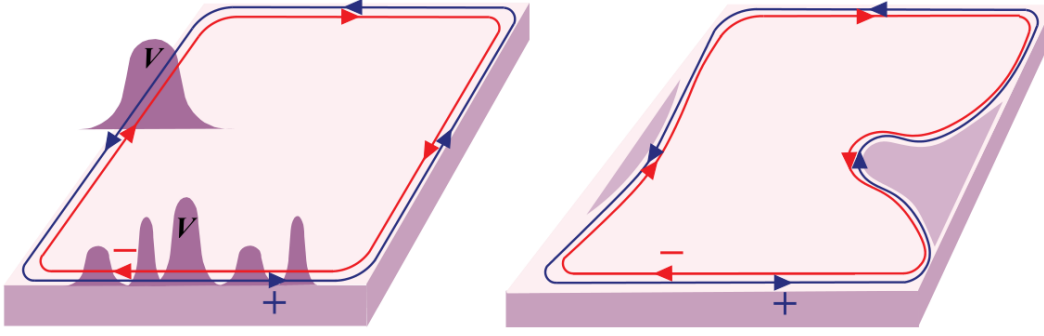
Figure 2.1.4: Protection of the edge states of the QSHE phase against a disorder potential or deformation. From [4].

$\hat{V}$. The scattering matrix element reads [4]:

$$\langle+|\,\hat{V}\,|-\rangle = \langle-|\,\mathcal{T}^{\dagger}\hat{V}\,\mathcal{T}^{-1}|+\rangle = -\langle-|\,\mathcal{T}^{\dagger}\hat{V}\,\mathcal{T}\,|+\rangle = \langle-|\,\mathcal{T}^{\dagger}\mathcal{T}\,\hat{V}\,|+\rangle$$

$$\tag{2.1.6}$$

$$= -\langle-|\,\hat{V}\,|+\rangle^{*} = -\langle+|\,\hat{V}^{\dagger}\,|-\rangle \tag{2.1.7}$$

Given that a an operator $\hat{V}$ representing a physical perturbation has to be hermitian, the matrix element can only be zero. The edge states are therefore protected against many ordinary perturbations such as surface disorder or defects, chemical doping or external electric fields, as shown on figure 2.1.4. Nevertheless, they are not protected against any kind of magnetic perturbation, like one created by depositing magnetic atoms on the surface. Indeed such an interaction is able to flip the spins of the electrons in helical states, and thus makes backscattering possible. By analogy with the quantum Hall effect, this electronic state is referred to as the *quantum spin Hall effect* (QSHE). However, since this phase respects the TRS, its topological properties cannot be described by the Chern number. It is therefore necessary to look for a new topological invariant to describe the QSHE.

The answer can be found in an algebraic property of the time reversal operator acting on Bloch wavefunctions, at some special points of the Brillouin zone [5]; but it is often hard to calculate. As for the Chern insulator, the meaning of the topological invariant is more easily explained in terms of bulk-boundary correspondence. Let us look at how the edge states, if present, can connect the time reversal symmetric points of the Brillouin zone, also called Kramers points. For a 2D system, the edge is 1D and there are only two such points in the Brillouin zone for the edge states:

the center and the edge. At the Kramers points, the Kramers doublet of edge states is degenerate; between those points, the degeneracy is lifted by the spin-orbit interaction. The topological character lies in how many times this pair of edge states crosses the Fermi level. If it is even, then the edge states can be adiabatically deformed so that there is no more crossing. But if it is odd, this operation is not possible. Therefore, the interface between two TRS phases, the bulk boundary correspondance can be expressed in the following form:

$$N_K = \Delta \nu \quad \mod \quad 2 \tag{2.1.8}$$

where N_K is the number of Kramers pairs of edge modes intersecting the Fermi level, and $\Delta \nu$ is the change in topological invariant at the interface. For example, the QSHE phase has one single Kramers doublet of edge states at the interface with the trivial vacuum; therefore, this phase is topologically non trivial. This number ν cannot take all integers values like the Chern number.It is only two-valued, and is thus coined the $\mathbb{Z}_2$ invariant. Its computation can be made simpler if the system has additional symmetries, such as preserving the perpendicular spin $\hat{\sigma}_z$ or crystalline inversion symmetry. These tricks are used extensively to find new topological insulators from band structure calculations. From now on, we will focus on 3D topological insulators.

2.1.3 3D topological insulators

Three dimensional topological insulators can be thought of as generalizations of spin Hall 2D topological insulators described above. The surface states on a 3D topological insulator are labelled by a 2D Brillouin zone, where there are 4 Kramers points Γ_1, Γ_2, Γ_3 and Γ_4 (shown on figure 2.1.5 (a) and (b)). As in the 2D case, the surface states are degenerate at the Kramers points, and between said points this degeneracy is lifted by the spin-orbit interaction. This means that the spectrum of the edge states at the Kramers points resembles the one of a spin $\frac{1}{2}$ particle obeying the 2D Dirac equation. Thus in 3D the Kramers points where there are edge states are also called Dirac points. Similarly to the 2D case, one can define $\mathbb{Z}_2$ invariants describing how many edge states cross the Fermi level between two Dirac points points Γ_i, Γ_j [5]. There are 6 such pairs of points but a geometry argument shows that only 4 $\mathbb{Z}_2$ invariants are independent; the interested reader may find more details in [16]. 3D topological insulators
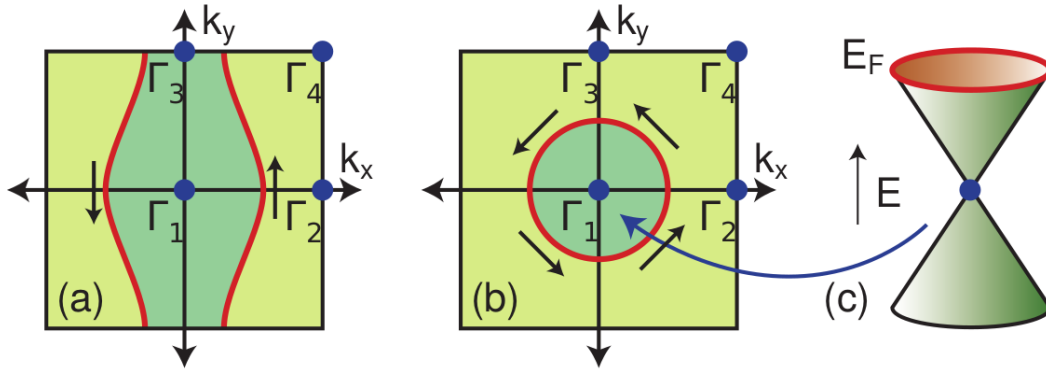
Figure 2.1.5: Brillouin zone at the Fermi level for the edge states for (a) a weak 3D topological insulator and (b) a strong topological insulator. From [5].

are thus characterized by 4 $\mathbb{Z}_2$ invariants $(\nu_0, \nu_1\nu_2\nu_3)$. The first one ν_0 is the one which has the most effect on the resulting electronic phase. It corresponds to the parity of the number of TRS points inside the Fermi circle.

The simplest topologically non-trivial 3D material can be constructed by stacking layers of 2D quantum spin Hall insulators. For instance, weakly coupling layers along the y direction can create the Fermi circle and spin polarization of edge states depicted on figure 2.1.5 (a). Therefore the ν_0 invariant for such a state is 0. But there are no surface states on the face perpendicular to the stacking axis, and on the other surfaces the edge states are not protected by time-reversal symmetry. They can exist on a clean surface but are easily localized in the presence of disorder. Such an electronic phase is called a weak topological insulator.

On the contrary, a phase with $\nu_0 = 1$ cannot be interpreted in terms of layers of 2D topological insulators. This phase is called a strong topological insulator and is characterized by an odd number of Dirac points inside the Fermi circle. The simplest case, where there is only one such point at the center of the Brillouin zone Γ_1, is depicted on figure 2.1.5 (b). The surface states are degenerate at Γ_1, and separated by spin-orbit interaction away from this point. Therefore, the Hamiltonian of the edge states close to the Dirac point is:

$$\hat{\mathbf{H}} = \sum_{\mathbf{k},\sigma} \Psi^{\dagger}_{\mathbf{k},\sigma} \hat{\mathscr{H}}(\mathbf{k}) \Psi_{\mathbf{k},\sigma} \tag{2.1.9}$$

$$\text{with} \quad \hat{\mathscr{H}}(\mathbf{k}) = \hbar v_f \hat{\sigma} \cdot \hat{\mathbf{k}} - E_f = \hbar v_f (\sigma_x k_x + \sigma_y k_y) - E_f \tag{2.1.10}$$

where $\Psi_{\mathbf{k},\sigma}$ is a spinor field operator for an electron, v_f is the Fermi velocity of charge carriers and E_f is the position of the Fermi level relative to the Dirac point. The corresponding band structure, shown on figure 2.1.5 (c), is linear:

$$E(\mathbf{k}) = \pm\hbar v_f |\mathbf{k}| \tag{2.1.11}$$

It is analogous to the Dirac dispersion relation, with v_f playing the role of the speed of light. The helical spin structure still provides topological protection against backscattering, but not against other scattering processes $\mathbf{k} \mapsto \mathbf{k}'$.

An experimental realizations of 3D topological insulators requires a compound with a large bulk band gap, at least 0.25 eV (or about 3000 K). The goal is to make the bulk conductivity as low as possible, so that measurements of surface transport are not degraded by parasitic leaks in the bulk. But this band gap must be smaller than the spin-orbit coupling energy. The idea is to use the spin-orbit interaction to create inversions of the bulk conduction and valence bands. If one imagines slowly turning on the spin-orbit interaction, the band gap will start to close with the separation of up and down spin bands, until it opens again into a topologically non trivial phase. Spin-orbit coupling being an effect of relativistic origin, it is more intense in using heavier elements. It can reach energies of about 1 eV using materials like antimony, bismuth, selenium or tellurium. Indeed, materials like Bi_2Se_3, Bi_2Te_3 or Sb_2Te_3 are strong topological insulators, with invariants (1, 000). Up to now, Bi_2Se_3 has been the most studied, because it has a larger band gap of about 0.3 eV and a band structure that resembles more the ideal case of equation (2.1.10). Owing to this, it has been used as a platform to demonstrate the main theoretical predictions of the field [5]. Its band structure and ARPES spectrum are depicted on figure 2.1.6. On subfigure (d) one can see that the surface state dispersion in real materials slightly departs from the ideal case: the particle-hole symmetry between the upper half and the lower half of the Dirac cone is broken. Tuning the Fermi level farther from the Dirac point, one can also see an hexagonal warping of the cone [5]. In addition, the topological surface states remain well-defined up to room temperature.

Most of the interesting theoretical and technological proposals require the Fermi level to be as close as possible to the Dirac point. As a matter of fact, figure 2.1.6 shows that the Fermi level of Bi_2Se_3 is not even in the bulk band gap. For ARPES measurements, this actually makes it possible to see a greater part of the surface states dispersion, given that
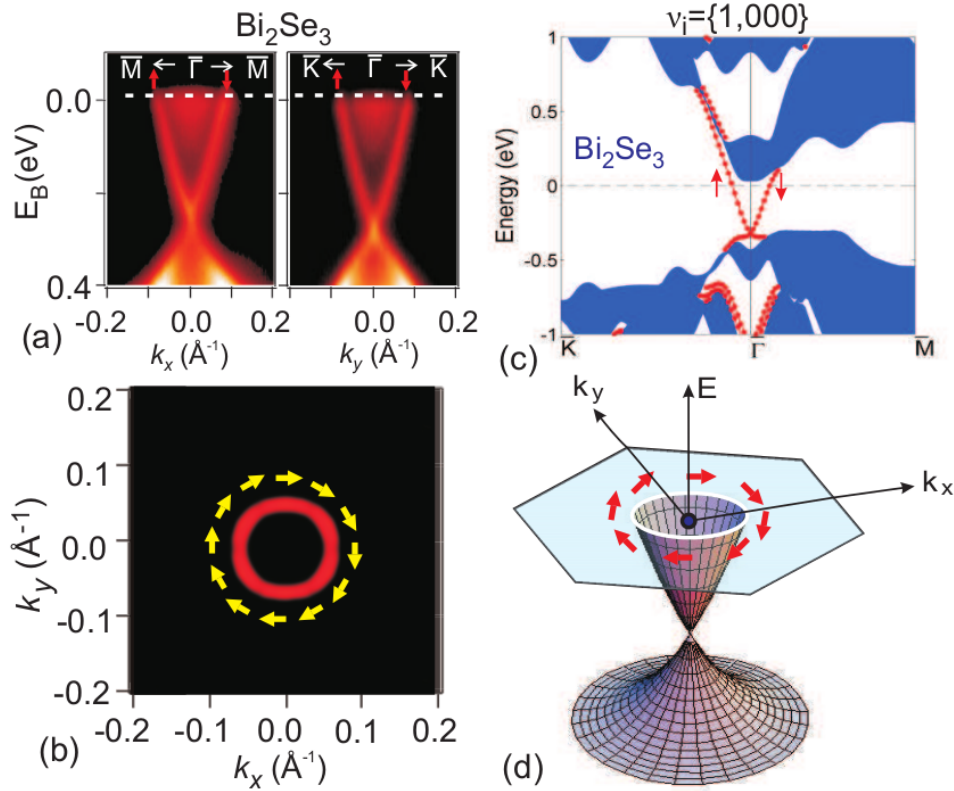
Figure 2.1.6: Surface states and band structure of strong topological insulators. (a) ARPES spectra of Bi_2Se_3 close to the Γ point, showing the surface state dispersion, very close to an ideal Dirac cone, and (b) their helical spin texture. (c) Band structure calculation along two directions of the Brillouin zone. The shaded regions describe bulk states, and the red lines are surface states. (d) General dispersion relation and spin texture for the edge states of Bi_2X_3 (1, 000) topological insulators. From [5].

this technique can only see occupied states. However it is a problem for most transport measurements or experiments in a magnetic field, where separating contributions of surface electrons from the one of bulk electrons is of crucial importance. One solution to change the position of the Fermi level is to modify the chemistry of the topological insulator, using for example a quaternary compound of the family $Bi_xSb_{2-x}Te_ySe_{3-y}$ (also known as BSTS). This chemical modification has an effect very similar to electronic doping [17]. For instance, in this family one can tune the position of the Dirac cone from 0.2 eV above the Fermi level (Sb_2Te_3) to more than 0.3 eV below ($Bi_2Te_{0.5}Se_{2.5}$). This phenomenon is highlighted in figure 2.1.7, showing two different samples of BSTS at equilibrium. However, even if the Dirac point is close to the Fermi level, it is still possible to reveal the top of the cone and the bottom of the conduction band with time resolved ARPES. Indeed, the nonequilibrium character of this technique means that it can populate states that were unoccupied before, as can be seen in figure 2.1.7.
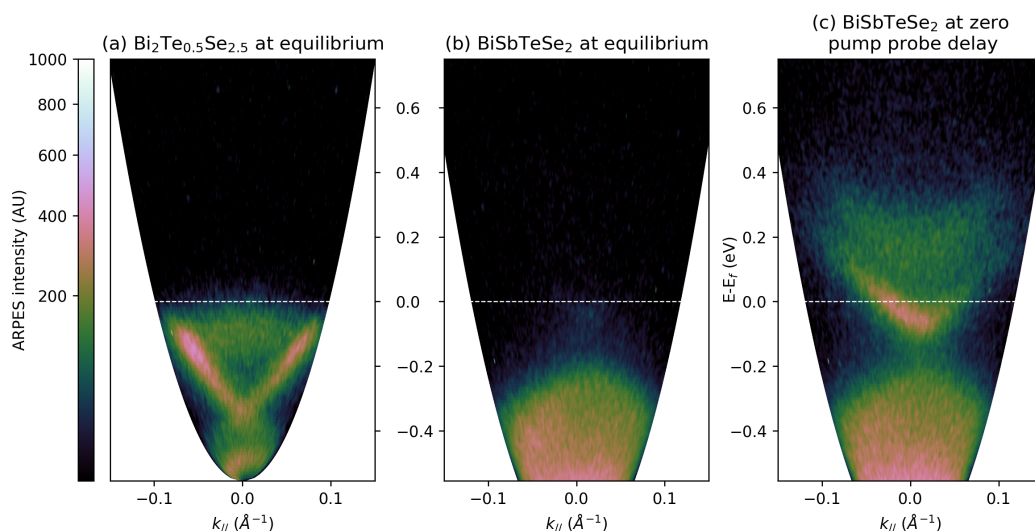
Figure 2.1.7: ARPES data at room temperature showing the different positions of the Dirac cone relative to the Fermi level, in (a) $Bi_2Te_{0.5}Se_{2.5}$ and (b) $BiSbTeSe_2$. (c) $BiSbTeSe_2$ at zero delay when the pump and the probe overlap, with a pump power of 6 mW. The Fermi level in marked with a white dashed line to guide the eye.

As an end note on the general concepts of topological insulators, one should note the difference between the *symmetry protected topological*

states described in this work, and phases with *intrinsic topological order* [18]. Topological order relies on long-range entanglement, which usually happens in strongly interacting phases, whereas topological insulators are described as free fermion systems. Both phases can exhibit protected gapless edge modes; but those in a topologically ordered phase are robust against *any* local perturbation, while in a topological insulator they are protected against local perturbations that do not break the symmetry. In addition, topologically ordered phases often exhibit exotic properties like fractionalized statistics or an emergent gauge theory, and this in a way depending on the topology of the manifold on which they are considered.

2.2 Dynamics of topological states in Bi$_2$Te$_2$Se

Understanding and controlling the dynamics of the topological states is of great importance in the development of TI-based electronic and spintronic devices. In this section, we explain how the TR-ARPES setup can reveal the different electronics dynamics in the topological insulator Bi$_2$Te$_2$Se. This compound has a Dirac point located about 0.3 eV below the Fermi level. We start by taking TR-ARPES snapshots of Bi$_2$Te$_2$Se every 50 fs with a pump power of 7 mW. Then, we define four energy-momentum regions in the band structure. They are represented as colored rectangles on the ARPES data in figure 2.2.1 (a), within which we integrate the ARPES signal at each time. The green and blue regions correspond to excited electrons in bulk conduction bands, respectively a high-energy conduction band (HCB) and the low-energy one which crosses the Fermi level (LCB). The orange and red regions correspond to electrons in the topological surface states (TSS). More precisely, the orange regions correspond to the parts of the Dirac cone above the Fermi level (TSS+), and the red one to parts below the Fermi level (TSS-). The evolution of the electron population in these regions are on figure 2.2.1 (b) and can help us understand the decay path of the electrons during and after photo-excitation.

First, we observe that the population of HCB (green) increases first, reaching its maximum in about 200 fs. The population of TSS+ (red) varies in an opposite way, reaching its maximum depletion in a similar
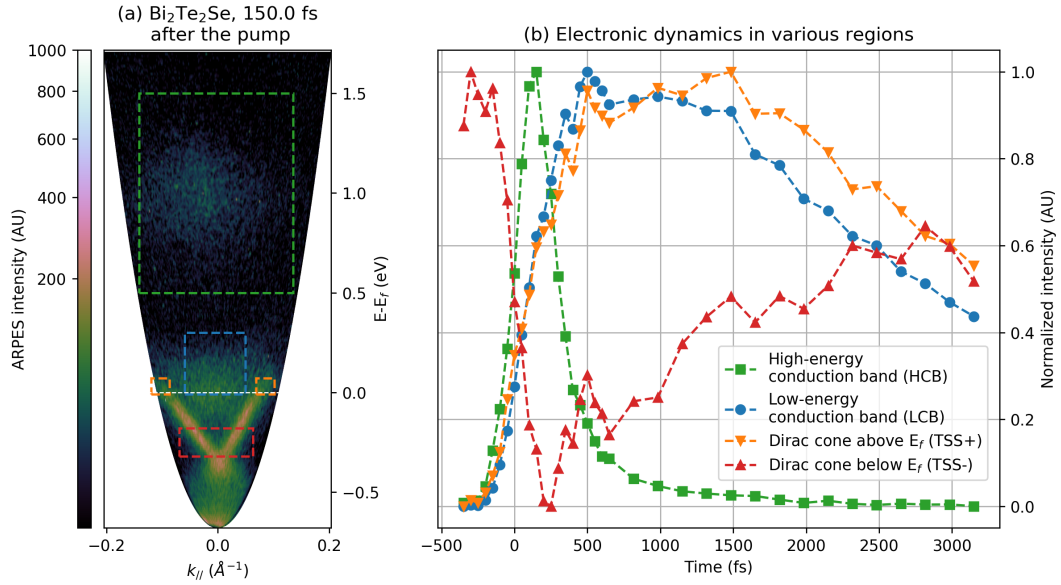
Figure 2.2.1: (a) ARPES data of Bi_2Te_2Se at room temperature 150 fs after the pump. The pump power is 7 mW. (b) Electronic dynamics of various zone of the band structure, shown as colored rectangles on panel (a). The curves have been normalized to their respective maxima and minima.

time. This indicates that the photo-excited electrons directly populate the HCB. The same depletion and population dynamics has been reported in Bi_2Te_3 [19]. In addition, the population of HCB shows the fastest decay, of around 500 fs. This fact can be simply understood in terms of the Fermi golden rule. The HCB has a higher energy than other regions, and therefore a particle excited there has more available states to decay into, thus increasing the decay rate [17]. Then, we notice that both the LCB (blue) and TSS+ (orange) regions have similar dynamics. The population build-up time of about 800 fs for both regions means that there is no clear evidence of a direct, photo-induced population in these regions. Instead, the low-energy bulk band and the surface band are populated mostly by the relaxation of electrons in the HCB, through inter-band scattering. After one picosecond, the HCB is almost back to its (empty) equilibrium state. The electrons then relax towards the Fermi level through intra-band scattering, mediated for instance by electron-phonon interaction. But these processes have a lower energy, which explains the longer build-up time. After about 1200 fs, the electrons just above the Fermi level (in TSS+ and LCB) start relaxing towards equilibrium. This process is mostly

driven by the recombination between electrons and holes, which can in this case be considered symmetric with respect to the Fermi level [19]. This can explain the opposite population slopes between TSS+ and TSS-after 1200 fs. Finally, we note that the relaxation of the LCB happens at the same rate of TSS+, only about 500 fs sooner. This may indicate that the bottom of the LCB acts as a charge reservoir, which in a way empties itself through the topological surface states. To sum up, we see that the TR-ARPES setup is able to measure the evolution of the population of various bands, which can help understand the flow of charge after photo-excitation.

2.3 Depositing magnetic impurities

Probing the effect of magnetic perturbations on the topological surface states can not only help develop new TI-based devices, but also pave the way for the realization of exotic particles such as axions on the surface [20]. This section focuses on the deposition of magnetic atoms on the topological insulator Bi_2Te_2Se, and the effect it has on the dispersion relations of the topological surface state. We choose to deposit atoms of cobalt, using the evaporator integrated in the experimental setup (section section 1.2). Indeed cobalt atoms have an intrinsic magnetic moment, of about 1.7 times the one of the electron. As explained in section 2.1.2, the topological surface states are not robust against scattering by a non time-reversal symmetric potential, such as the one created by a magnetic field. However, the effect of a random deposition of magnetic atoms on the edge state dispersion is not straightforward to derive. To understand the collective behavior of the magnetic impurities, theoretical studies [21, 22] have investigated the interplay between those impurities and electrons on a Dirac cone with a helical spin texture. They found that the classic RKKY interaction between the spins of the impurities, when mediated by such electrons, amounts to an anisotropic ferromagnetic interaction between the impurities, which favors ferromagnetic ordering of the spins perpendicularly to the surface. The effect of a high density of magnetic impurities can therefore be modeled by adding to the Hamiltonian 2.1.10 a term corresponding to an effective magnetic field perpendicular to the surface: $\hbar B_z \sigma_z$. However, to keep the analogy with relativistic physics, we will refer to this term as a *mass term* $m v_f^2 \sigma_z$, as this Hamiltonian corresponds to the one of a massive Dirac

particle. In the end, we get the following Hamiltonian for the surface states:

$$\hat{\mathcal{H}}(\mathbf{k}) = \hbar v_f (\sigma_x k_x + \sigma_y k_y) + m v_f^2 \sigma_z - E_f \tag{2.3.1}$$

and surface band dispersion [4]:

$$E(\mathbf{k}) = \pm\sqrt{(\hbar v_f |\mathbf{k}|)^2 + (m v_f^2)^2} - E_f \tag{2.3.2}$$

Therefore the mass term opens a gap of value $2m v_f^2$ at the Γ point. Our goal will now be to measure accurately the gap and the Fermi velocity for Bi_2Te_2Se with and without cobalt.
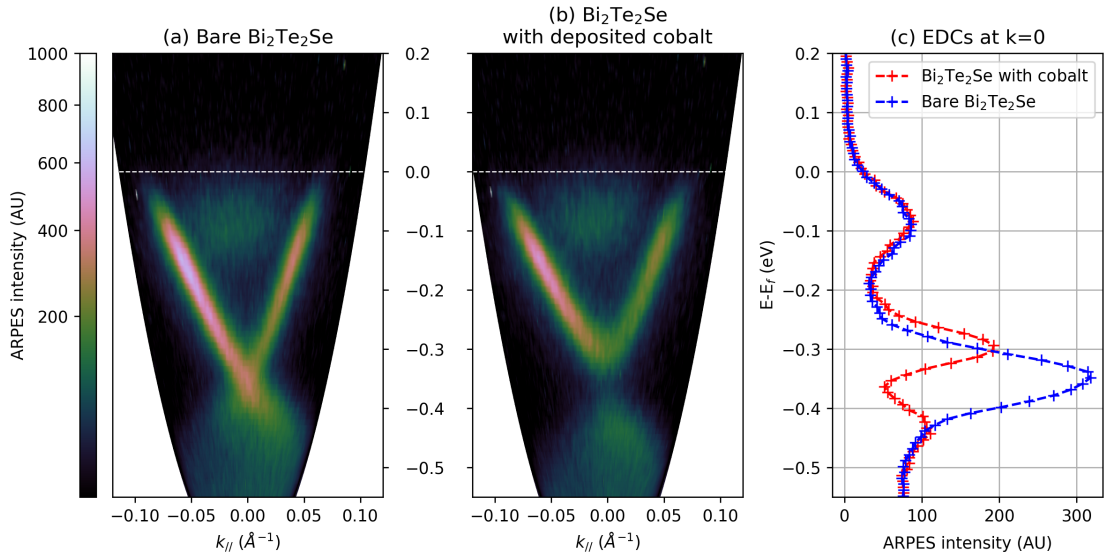
Figure 2.3.1: Comparison between (a) bare Bi_2Te_2Se and (b) Bi_2Te_2Se with deposited cobalt. The sample was exposed during 30 seconds to cobalt evaporated with an emission current of 7 mA. (c) EDCs for both samples at $k_\parallel = 0$.

Figure 2.3.1 compares the equilibrium ARPES signal of bare Bi_2Te_2Se (panel (a)) to Bi_2Te_2Se with deposited cobalt (panel (b)). A gap opening of about 150 meV can clearly be seen. The EDCs at the Γ point for both situations are represented on panel (c). They show that as expected, the bulk bands above and below the Dirac point are not essentially affected by the surface impurities. To measure the gap more precisely, we will follow the procedure below:

- Take EDCs at various $k_\parallel$ values for both situations (without and with cobalt),

- Fit the EDCs with an appropriate fitting function and find the position of the surface state at each $k_\parallel$,

- Fit the surface states dispersion with the corresponding dispersion relation (respectively equation (2.1.11) and equation (2.3.2)),

- Compare the results of the fits to find the value of the gap opened by the cobalt atoms.

In this case, as the bands we want to fit are quite narrow in energy, we will use a simple Gaussian line shape. For each EDC, the location of the surface state is defined to be the center of the gaussian given by the fit routine. Furthermore, we will focus our analysis where the data is of the best quality, i.e. on the top left part (negative $k_\parallel$) of the Dirac cone. The symmetries of the gap opening ($\pm m$ from the Dirac point) and of the band structure $E((k)) = E(-(k))$) ensure that this restriction is meaningful. The results of this analysis are presented in figure 2.3.2. The EDCs taken from $k_\parallel = -0.55\,\text{Å}^{-1}$ to 0 for both situations are shown in panels (a) and (b). The blue and red dots correspond to the location of the surface states as defined earlier. The locations of the surface states are again shown in panel (c), along with the corresponding fits with the dispersion relations 2.1.11 and 2.3.2. According to these fits, the opened gap is about 130 meV, corresponding to a mass of about 4% of the one of the electron. These values are consistent with similar measurements with iron deposition [23]. More surprisingly, the cobalt deposition seems to lower slightly the Fermi velocity; from $v_f = 5.7\cdot10^5\,\text{ms}^{-1}$ for bare Bi_2Te_2Se to $5.2\cdot10^5\,\text{ms}^{-1}$ for Bi_2Te_2Se with cobalt. Such a drop in the Fermi velocity can originate from the application of a perpendicular electric field [24], which can be caused by atoms deposited at the surface [25]. But further investigation is needed to conclusively answer this question.

To summarize, we have seen how the TR-ARPES data can be analyzed to find numerical values of band gaps or of parameters of the electronic Hamiltonian. The next step in the study of topological insulators with a magnetically doped surface is the analysis of the dynamics of the gapped surface states, in a way similar to what has been done in section 2.2. Unfortunately the corresponding experiments could not be realized during the internship, due to a succession of problems in the experimental setup.
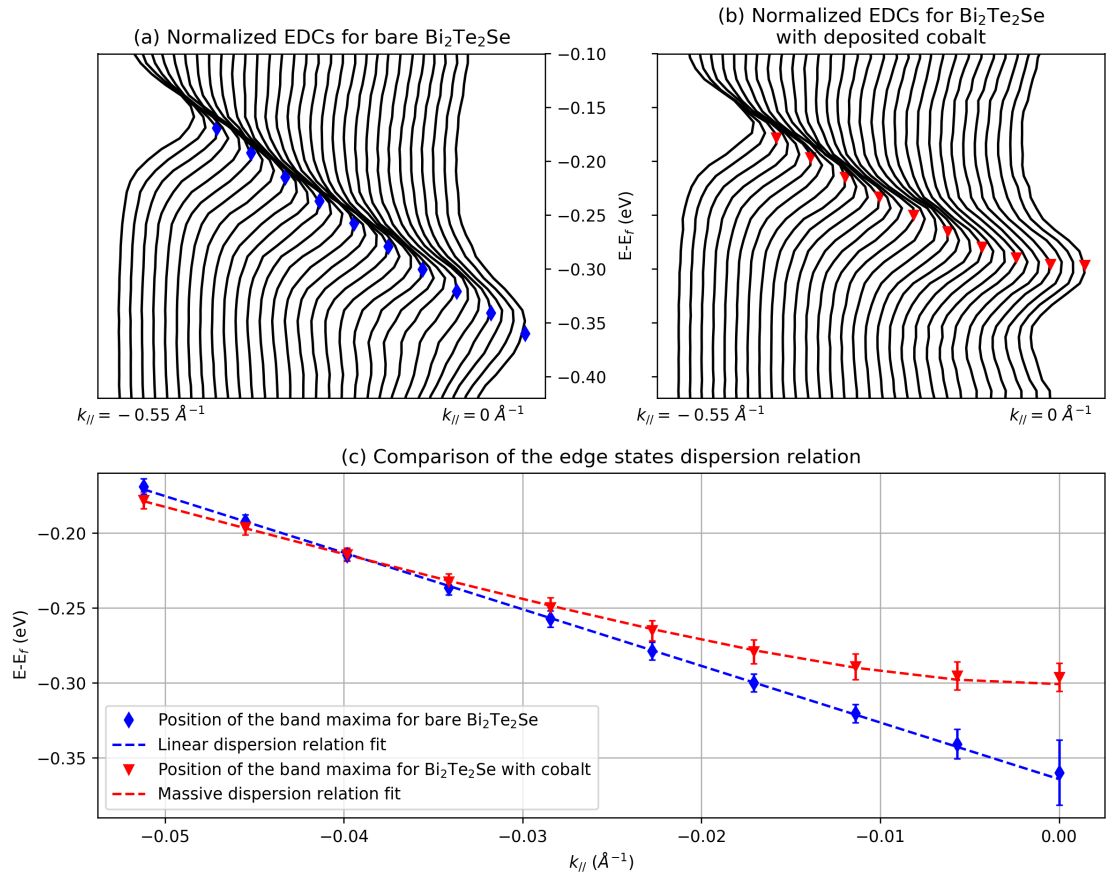
Figure 2.3.2: Waterfall plot of the normalized EDCs at various $k_\parallel$ for (a) bare Bi_2Te_2Se and (b) Bi_2Te_2Se with cobalt. The colored points correspond to the location of the surface state for some EDCs. (c) Comparison of the surface state dispersion for both cases. The error bars correspond to the 95% confidence interval on the location of the surface states with a gaussian fit; they are taken into account in the fits by the theoretical models (dashed lines).

3 Electronic dynamics of a charge density wave compound: 1T-TaSe$_2$

In this section, we study the ultrafast electronic dynamics of 1T-TaSe$_2$. This material presents a rich landscape of correlated phases, among which charge density waves and metal-insulator transitions.

3.1 Origins of charge density wave transitions

Metals usually have a very uniform electron density. But in some materials, the Fermi surface may become unstable below a critical temperature T_c. This instability can lead to a redistribution of the electron density, where it is modulated spatially according to a given wave vector **s**. This new phase is called a charge density wave (CDW). The modulated electron density modifies in return the potential around the ions, which also shift them into new equilibrium positions. Thus a CDW is always accompanied by a lattice distorsion. The electron modulation and lattice modulation can have rational or irrational ratios, in which case the CDW state is called commensurate (CCDW) or incommensurate (ICCDW) respectively.

CDW formation is a complex phenomenon and does not seem to be caused by only one mechanism. Nevertheless, we can highlight some important features of most CDW states using a 1D picture: the Peierls distorsion. Let us consider a 1D chain of atoms with lattice constant a and one electron per atom, as shown in figure 3.1.1 (a). This system is a metal and the corresponding band structure is shown in panel (c). But by doubling the lattice constant and introducing two different hopping amplitudes for the electron (panel (b)), it is possible to lower the energy of the entire electronic structure by opening a gap at the Fermi level (panel (d)). In this model, the CDW is therefore always linked to a metal-insulator transition.

The cause of this instability in this 1D system is the divergent susceptibility for perturbations with a wave vector $\mathbf{q} = 2\mathbf{k}_f$. Such a divergence happens when parts of the Fermi surface can be matched upon translation by a vector $\mathbf{q}$ in reciprocal space. This feature is called Fermi surface nesting, and $\mathbf{q}$ is then referred to as the nesting or spanning vector. In this sense, the 1D Fermi surface of a linear chain (figure 3.1.1 (c)) is perfectly nested since it consists of only two points separated by $\mathbf{q} = 2\mathbf{k}_f$. This 1D picture can explain the CDW transitions in some materials, but it presents some limitations: no system is perfectly 1D, and most importantly some CDW transitions are not accompanied by a metal-insulator transition.
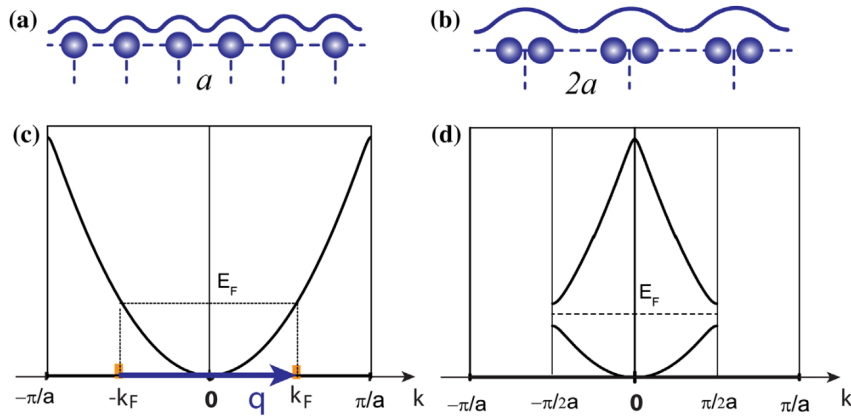
Figure 3.1.1: The Peierls distortion, a 1D picture of a CDW phase. (a) Regular 1D lattice of atoms. (b) Distorted lattice with doubled periodicity. (c) Band structure and Fermi points at half filling. $\mathbf{q}$ is the nesting vector. (d) Band structure in the distorted phase, showing the gap opening and the reconstructed Brillouin zone of half the original size. From [6].

In order to extend this description to 2D systems, one needs to take into account the renormalization of the phonon dispersion $\omega(\mathbf{q})$ by the electron-phonon coupling. The electron-phonon system is described by the Frölich Hamiltonian [6]:

$$\hat{\mathbf{H}} = \sum_{\mathbf{k}} \varepsilon(\mathbf{k}) \hat{a}_{\mathbf{k}}^{\dagger} \hat{a}_{\mathbf{k}} + \sum_{\mathbf{q}} \hbar\omega(\mathbf{q}) \hat{b}_{\mathbf{q}}^{\dagger} \hat{b}_{\mathbf{q}} + \sum_{\mathbf{k},\mathbf{q}} g(\mathbf{q}) \hat{a}_{\mathbf{k}+\mathbf{q}}^{\dagger} \hat{a}_{\mathbf{k}} \left(\hat{b}_{-\mathbf{q}}^{\dagger} + \hat{b}_{\mathbf{q}} \right) \qquad (3.1.1)$$

The first term corresponds to a free electron gas with dispersion $\varepsilon(\mathbf{k})$ and the second to the free phonons with energy $\hbar\omega(\mathbf{q})$. The last term models the electron-phonon coupling with a momentum-dependent coupling $g(\mathbf{q})$. This coupling renormalizes the bare phonon dispersion $\omega(\mathbf{q})$ in the

following manner:

$$\tilde{\omega}(\mathbf{q})^2 = \omega(\mathbf{q})^2 + 2\omega(\mathbf{q})\big|g(\mathbf{q})\big|^2 \mathrm{Re}\left[\chi(\mathbf{q}, \omega)\right] \tag{3.1.2}$$

where $\chi(\mathbf{q}, \omega)$ is the interacting susceptibility function. This function is both difficult to calculate and to measure experimentally, so we will approximate it by its non-interacting counterpart, also called the Lindhard function $\chi_0(\mathbf{q}, \omega)$. Its real part is negative and can be expressed as:

$$\mathrm{Re}\left[\chi_0(\mathbf{q}, \omega)\right] = \frac{-2}{(2\pi)^2} \int\limits_{\mathrm{BZ}} \frac{f_{\mathrm{FD}}(\mathbf{k}) - f_{\mathrm{FD}}(\mathbf{k} - \mathbf{q})}{\hbar\omega + \varepsilon(\mathbf{k}) - \varepsilon(\mathbf{k} - \mathbf{q})} \tag{3.1.3}$$

where f_{FD} is the Fermi-Dirac distribution. When $\mathbf{q}_n$ is a nesting vector, then by definition $\varepsilon(\mathbf{k}) - \varepsilon(\mathbf{k} - \mathbf{q}_n)$ is almost 0 on a large part of the Brillouin zone, which increases the absolute value of $\mathrm{Re}\left[\chi_0(\mathbf{q}_n, \omega)\right]$. This in return lowers the frequency of the renormalized phonon at $\mathbf{q}_n$, which is called the Kohn anomaly. If the nesting is large enough, the renormalized frequency of the phonon at $\mathbf{q}_n$ becomes imaginary ($\tilde{\omega}(\mathbf{q}_n)^2 < 0$), meaning that a static lattice distortion appears. Thus in this model, a large Fermi surface nesting can lead to an electronic instability and a CDW transition. But this mechanism can only explain a part of the observed CDW transitions, as some materials have Kohn anomalies without any significant Fermi surface nesting or CDW driven by electron-electron interactions[6].

3.2 Material properties of 1T-TaSe$_2$

Tantalum diselenide (TaSe$_2$) is part of a large family of compounds called transition metal dichalcogenides (TMDs), of formula MX$_2$ (M = Ti, Mo, W, Ta…, and X = S, Se, Te). As for graphene, these materials are composed of layers linked by a weak van der Waals interaction. The layers can exist in two different stacking arrangements called polytypes 1T (tetrahedral) and 2H (hexagonal), shown in figure 3.2.1 (a). Transition metal dichalcogenides have numerous applications in photonics, opto-electronics or even nanomedicine. But a lot of compounds in this family also exhibit a wide range of correlated electronic phases: superconductivity, metal-insulator transitions and charge density waves transitions. Such complexity makes it relevant to drive the compounds far from equilibrium with intense ultrafast laser pulses, to possibly switch between different

phases and study their recovery. Although 1T-TaS$_2$ has already been studied under this approach [26], there are few similar experimental works for 1T-TaSe$_2$, especially at low temperature.

1T-TaSe$_2$ forms a ICCDW below 600 K, then undergoes a first-order transition to a CCDW at 473 K. The commensurate phase is characterized by an electron density modulation and corresponding periodic lattice distortion (PLD) of size $\sqrt{13} \times \sqrt{13}$ in unit cell length. The reconstructed lattice, represented in figure 3.2.1 (b), follows a pattern of 13 Ta atoms star-of-David supercells, where 12 out the 13 atoms are displaced inwards. The PLD and CDW amplitudes are quite large compared to other TMDs: respectively 7% of the lattice constant and about 0.5 electrons per Ta atom [9]. The band structure of 1T-TaSe$_2$ has large elliptical electron pockets centered around the M points of the Brillouin zone, which are prone to Fermi surface nesting. Their approximate shapes at the Fermi level are shown in figure 3.2.1, with possible nesting vectors indicated as red arrows. The gap opened by the CCDW transition in the electron pockets is at about $0.8\,\text{Å}^{-1}$ from the Γ point, and is therefore not visible with the probe energy of our setup, which can access states with $\left| k_\parallel \right| \lesssim 0.1\,\text{Å}^{-1}$ at the Fermi level in this material. Other studies with a higher energy probe (for example, 22.4 eV in [8]) can map a part of the Brillouin zone large enough to observe the CDW gap and the folding of the band structure caused by the reconstruction of the lattice. To determine the orientation of the sample and the direction of the Brillouin zone probed by ARPES, a LEED pattern was taken (panel (d)). The hexagonal symmetry of 1T-TaSe$_2$ is clearly revealed by the high-intensity diffraction spot and highlighted with an orange hexagon. Its vertices are the center of a unreconstructed (no CDW) Brillouin zone. The reconstruction corresponds to the weaker pattern of the same symmetry (underlined with a blue hexagon). Comparing the sizes of the two patterns leads to a ratio ($720/200 \approx 3.6$) close to the predicted $\sqrt{13}$. The TR-ARPES setup will probe the band structure along the horizontal axis of the LEED pattern, emphasized with the white arrow, which turns out to be close to the $\Gamma - M$ direction of the Brillouin zone. In addition to modifying the diffraction pattern, the periodic lattice distorsion below 473 K creates new phonon modes in the extended star-of-David unit cell. Some of these phonons can be seen by Raman spectroscopy [27]: below the transition temperature, new peaks appear on the signal (panel (e)). The CDW phonon around 2.1 THz (70 cm^{-1}), of symmetry A_{1g}, will be of particular importance later. In the CCDW phase,

its frequency decreases with temperature, as shown on panel (f).
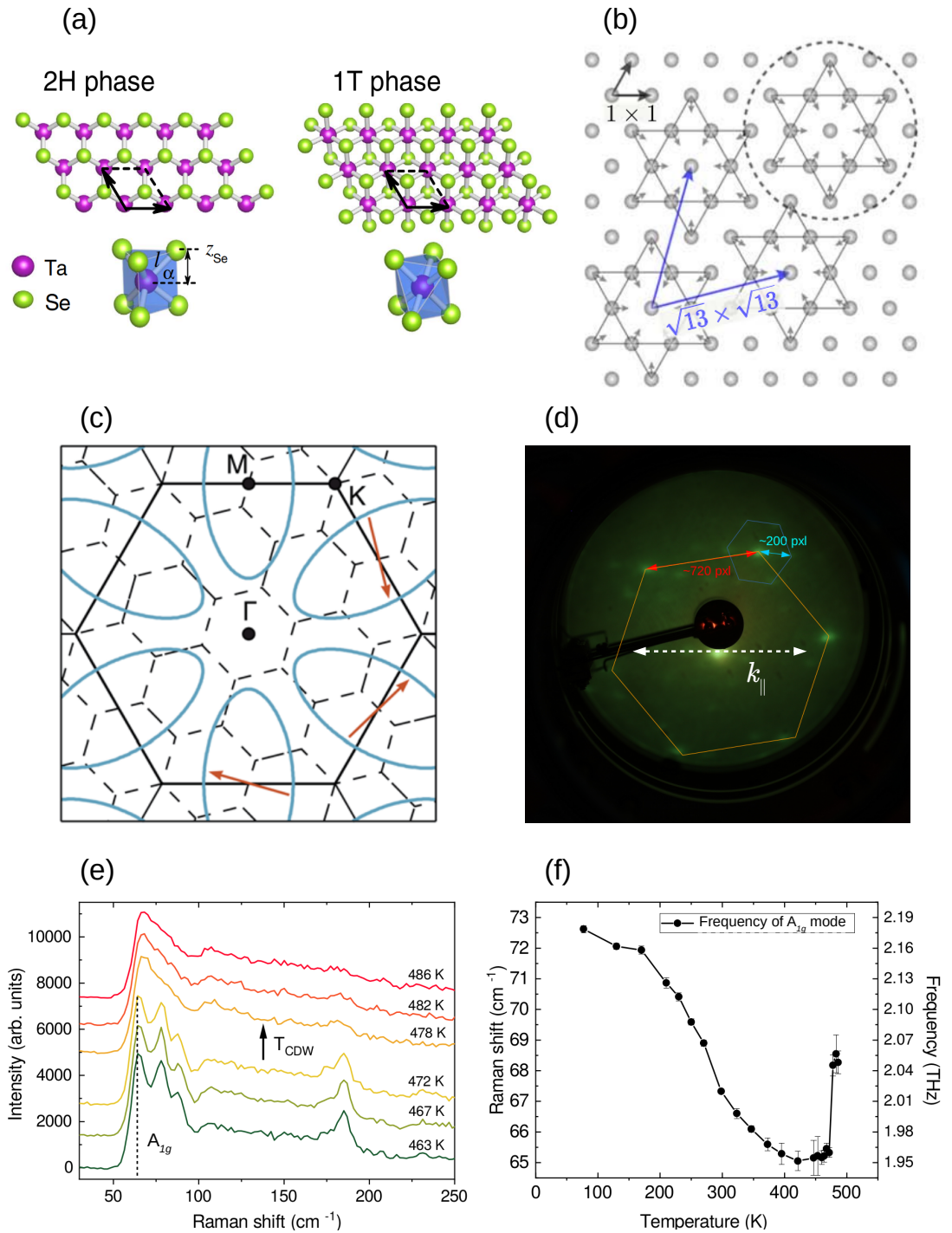
Figure 3.2.1: Structure and physics of TaSe$_2$. (a) The polytypes 1T and 2H of TaSe$_2$. From [7]. (b) Lattice reconstruction of 1T-TaSe$_2$ in the commensurate CDW phase. From [8]. (c) 2D band structure at the Fermi level. Blue ellipses indicate electron pockets, with possible nesting vector shown with red arrows. The dashed hexagons represent the reconstructed Brillouin zone. From [9]. (d) LEED pattern of the sample in the configuration used for all the experiments. (e) Raman spectra at temperatures near the ICCDW to CCDW transition. The dashed line indicates the phonon mode A_{1g} of interest. (f) Evolution of the frequency of the low-frequency A_{1g} mode with temperature. Figures (e) and (f) are courtesy of Charles Sayers.

Below about 200 K, 1T-TaSe$_2$ undergoes a metal-insulator transition which opens a Mott gap across the entire Fermi surface. This indicates that 1T-TaSe$_2$ exhibits strong electron-electron Coulomb coupling, in addition to the electron-lattice coupling relevant to the CDW transition. Figure 3.2.2 compares the equilibrium ARPES signal at 80 K (panel (a)) and room temperature (panel (b)). A gap opening of a few hundreds meV can clearly be seen. TR-ARPES with a probe energy of 6 eV is therefore perfectly suited to study the dynamics of the Mott phase around the Γ point. To get a more accurate value of this gap, one needs to define precisely the position of the band edges at the Γ point. High-energy ARPES [8, 9] and transport measurements reveal that the room temperature band touches the Fermi level, meaning that we can fit the edge with a Fermi-Dirac distribution. The resulting Fermi level is shown on the room temperature EDC as a blue dashed line in figure 3.2.2 (c), and is used as a reference for 0 binding energy. The low temperature band is much farther from the Fermi level so its spectral shape shows no influence of the Fermi-Dirac distribution. Therefore, the band edge at low temperature is defined as the maximum of the slope of the EDC while going down in energy. It is depicted as a red dashed line on panel (c). Defined this way, the gap opened is of about 300 meV. We will now focus on the electronic dynamics of 1T-TaSe$_2$ at room temperature, then in the Mott phase at 80 K.
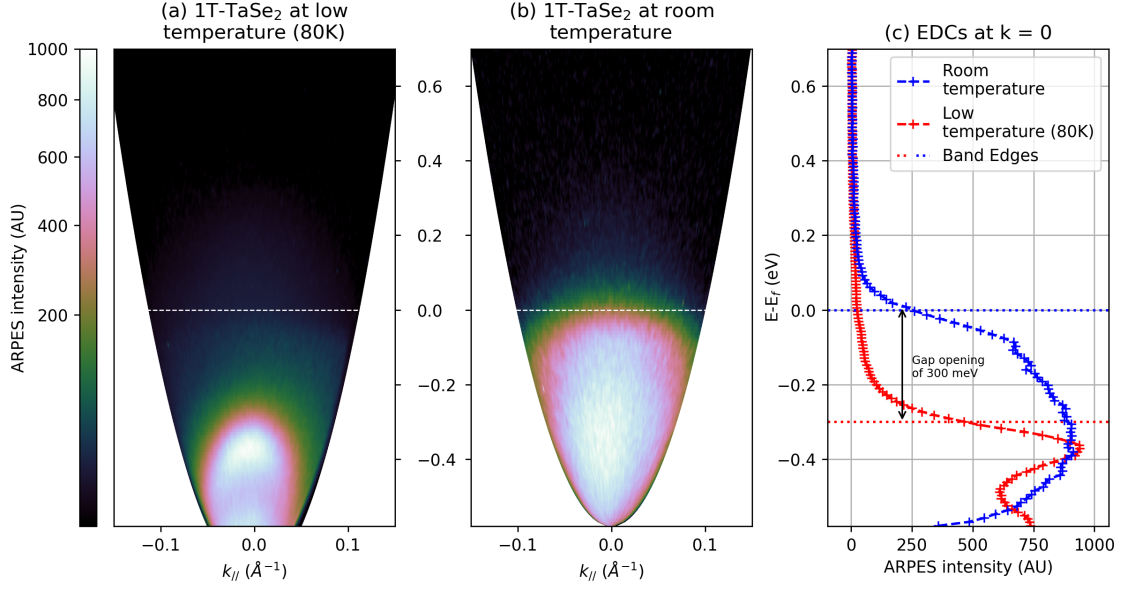
Figure 3.2.2: Comparison of the equilibrium ARPES signal of 1T-TaSe$_2$ at 80 K (panel (a)) and room temperature (panel (b)). The Fermi level is indicated with a white dashed line to guide the eye. (c) EDCs at $k = 0$ and position of the band edges at both temperatures.

3.3 Dynamics at room temperature

In this section, we investigate the dynamics of of 1T-TaSe$_2$ at room temperature, following a pump of 3.2 mW. ARPES snapshots are taken every 50 fs between -300 and 2000 fs, then every 500 fs until 5.5 ps. To make any kind of quantitative analysis, we first need to choose a spectral line shape that fits the data at all delays. The single band seen on the ARPES signal at room temperature is quite broad in energy, and intercepts the Fermi level. Therefore, a fit with a product of a Lorentzian and the Fermi-Dirac distribution should be able to reproduce the features of the EDC.

$$EDC = \frac{A_0 \gamma^2}{(E - E_0)^2 + \gamma^2} \cdot \frac{1}{1 + e^{\frac{E - \mu}{k_B T}}} \qquad (3.3.1)$$

In order to ensure that the fit results are physically relevant, we can define physically meaningful constraints on the fit parameters. In our case, there is no reason for the Fermi level μ to move over time, so it is kept at

0. Moreover, we can also expect the width of the Lorentzian γ to increase during and just after the pump, then exponentially decay to its equilibrium value. Indeed, the width of the Lorentzian is related to the lifetime of quasiparticles, and this behavior is something which is commonly seen in TR-ARPES. Figure 3.3.1 presents the results of this analysis. Panels (a) and (b) compare the ARPES signal at equilibrium and after 100 fs after the pump respectively, to highlight the photo-excited states. The evolution of the EDCs at $k = 0$ is represented on panel (c). The black line corresponds to the equilibrium EDC, taken 300 fs before the pump. EDCs from 0 delay (in blue) to 800 fs after the pump (in green) show one of the main features appearing in most TR-ARPES experiments: the slope of the band edge at the Fermi level increases just after the pump, then relaxes back to equilibrium. This indicates a similar evolution in the electronic temperature. Indeed, panel (d) shows the evolution over time of the effective electronic temperature T_{eff}, defined to take into account the broadening caused by the instrument resolution [3]:

$$T = \sqrt{T_{eff}^2 + \left(\frac{\Delta E_{exp}}{4k_B}\right)^2} \qquad (3.3.2)$$

ΔE_{exp} is set so that the equilibrium effective temperature matches the known experimental temperature of 300 K. As expected, T_{eff} first presents a sharp increase during the pump, then decays back with a time constant of about 500 fs, typical of many materials for photo-excited states. Finally, panel (e) depicts the evolution of the binding energy of the band maxima $E_0(t)$ compared to its equilibrium condition. Although this parameter has a larger uncertainty, it seems to present a downward shift on which are superimposed oscillations. Since no Mott or CDW gap is expected at Γ at this temperature, the apparent downward shift is probably just an artifact resulting from the displacement of electrons above E_f caused by the pumping. The oscillations are a more intriguing feature. The data can be correctly fitted between 0.5 and 1 ps by the sum of a sine and an exponential decay with the same time constant as for the effective temperature (panel (d)). The frequency of the oscillations is found to be about 2.1 THz, which is close to the frequency of the A_{1g} CDW phonon at room temperature (figure 3.2.1 (f)). This is likely a signature of strong electron-phonon coupling, consistent with the Fermi surface nesting picture for CDW transitions. The quality of the data and the fits did not make it possible to estimate the characteristic damping time of the oscillations,

but similar experiments on 1T-TaSe$_2$ at room temperature seem to show that all oscillations disappear within 3 ps [8]. In order to get a clearer picture of the oscillations, we now study the dynamics of this compound at low temperature.
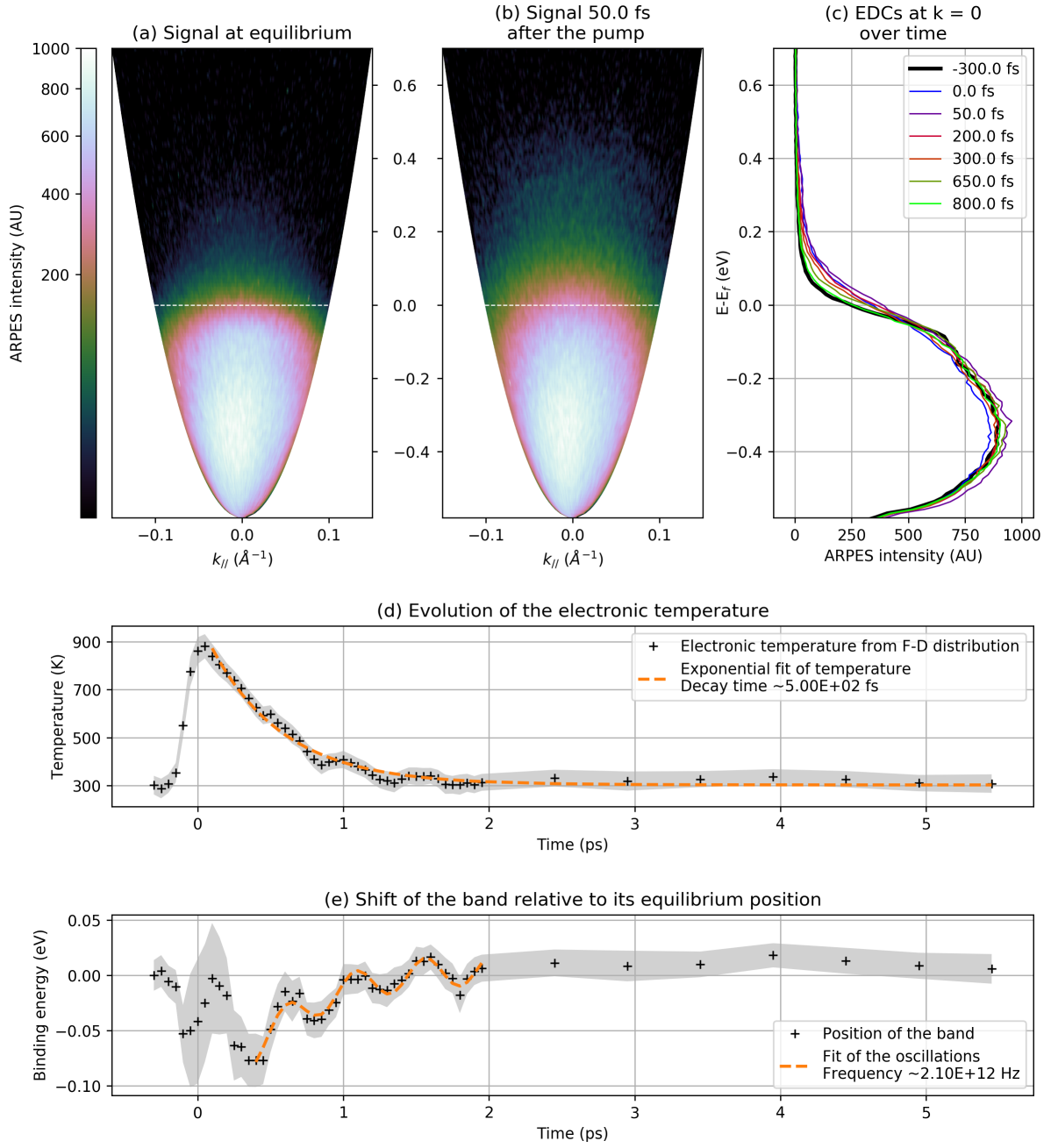
Figure 3.3.1: Electronic dynamics of 1T-TaSe$_2$ at room temperature. (a) ARPES signal at equilibrium and (b) 50 fs after the pump. (c) EDCs at $k_\parallel = 0$ over time. Colors from blue to red to green indicate increasing delays. (d) Dynamics of the effective temperature T_{eff} defined in the text, with a exponential decay fit. (e) Dynamics of the shift of the band relative to its equilibrium position, with a fit of the oscillations. The shaded areas on panels (d) and (e) are the confidence interval at 95% given by the Lorentzian × Fermi Dirac fit. They are taken into account for the fits of the temperature and the oscillations.

3.4 Dynamics at low temperature

In addition to the Mott gap opening, the low temperature (80 K) ARPES signal presents two distinctive bands, which we label upper and lower valence bands with respect to their energy (figure 3.4.1 (b)). These bands are much sharper and seem to be more dispersive than the broad room temperature band, which was very flat around Γ. In order to reproduce the main features of the dynamics in this regime, we choose to fit those two bands by a sum of two Voigt functions. The Mott gap opening pushes the bands far below the Fermi level compared to the thermal energy, so it is not necessary to take into account the Fermi-Dirac distribution. We use the same sampling rate as for the room temperature experiments, but using various pump powers: 1.6, 3.2, 6 and 8.1 mW. Figure 3.4.1 presents the evolution of important features of the two bands with a pump of 8.8 mW, where the nonequilibrium effects are the most visible. In panel (a), the EDCs at $k_\parallel = 0$ are represented for all delays with the same color map as the full ARPES maps. Oscillations of the entire band structure are clearly visible, but cannot be seen after 2 ps because of the sampling rate change. Panel (b) compares the same EDCs in a way similar to figure 3.3.1 (c). Contrary to the room temperature case, the slope of the band edge doesn't vary significantly. Instead, the edge appears to shift upwards by about 40 meV. This visualization also highlights the depletion of the two bands, seen as the transient decrease in intensity of the peaks. The shifts in the position of the two peaks relative to their equilibrium position are shown in panel (c). Both bands shift upwards about 100 meV after the pump, with the lower band (red) seemingly shifting upwards about 15 meV more than the upper band. They then decay back to equilibrium in a characteristic time of about 1 ps, of the same order of magnitude than the room-temperature case. The depletion dynamics (panel (d)) shows a similar temporal behavior. However, the most striking feature remain the oscillations superimposed to the band shift in panel (c). They are in phase for both bands and have a peak-to-peak amplitude of around 30 meV for a pump power of 8.8 mW. No decay can be seen in the oscillations up to 2 ps. An experiment over 17 ps with a pump power of 9.3 mW was attempted to find the damping time of oscillations. It showed that the oscillations persist up to at least 6 ps, but due to instabilities in the laser the data could not be properly analyzed.
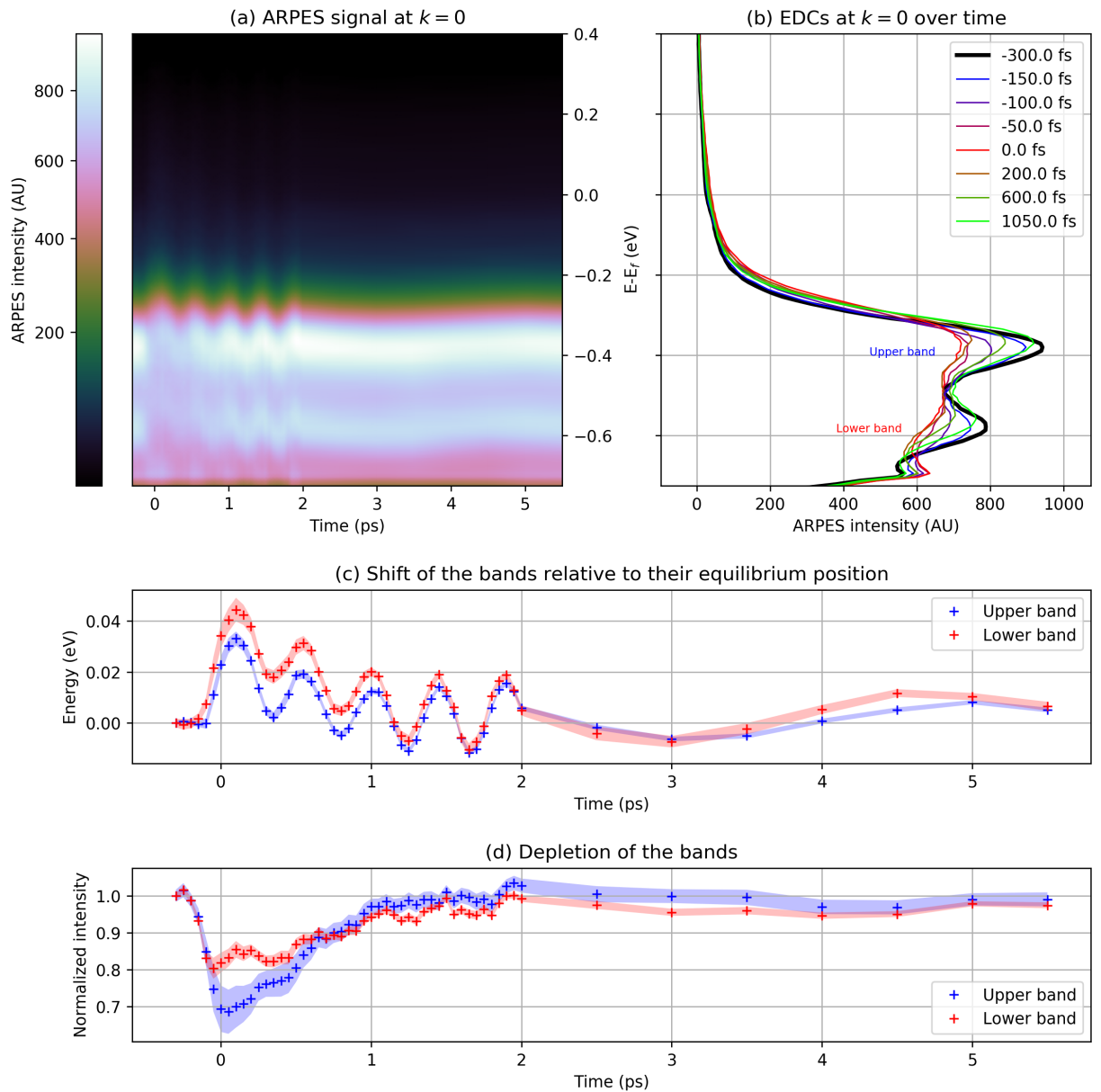
Figure 3.4.1: Electronic dynamics of 1T-TaSe$_2$ at 80K. (a) ARPES signal at $k_\parallel = 0$ over time. (b) EDCs at $k_\parallel = 0$ over time. Colors from blue to red to green indicate increasing delays. (c) Shifts of the positions of the maxima of the two bands relative to their equilibrium position. (d) Depletion of the two bands. The shaded areas on panels (c) and (d) are the confidence intervals at 95% given by the Voigt functions fit.

We now shift our focus to the systematic study of the oscillations in the upper band, since the Voigt fit is of better quality for this band. The

upper band shifts for all pump powers are shown in figure 3.4.2(a). We fit the oscillations between 1 and 2 ps with an undamped sine function, and report the frequency, peak-to-peak amplitude and phase for each pump power on figure 3.4.2, respectively on panels (b), (c) and (d). For all pump powers, the frequency of the oscillations have the same phase $-30°$ and frequency 2.3 THz, within confidence intervals. This frequency is once again close to the frequency of the A_{1g} phonon seen by Raman spectroscopy (figure 3.2.1 (f)): 2.19 THz at this temperature. Such long-lived oscillations at a phonon frequency are a signature of *coherent phonon oscillations*. In this phenomenon, the **q** = 0 mode of an optical phonon becomes macroscopically and coherently populated after excitation by an ultrafast laser pulse, in a way similar to Bose-Einstein condensation [28]. We therefore have strong evidence to affirm that the Mott phase of 1T-TaSe$_2$ is coupled to a CDW phonon, the A_{1g} mode at 2.2 THz, which modulates the band gap. In addition, the maximum band shift did not exceed 30 meV for the upper band, about 10% of the Mott gap. This means that even at the maximum pump power we used, the Mott phase is only weakly disturbed and most of the energy of the excitation is in the form of a large lattice displacement. Besides, the amplitude of the oscillations increases more or less linearly with the pump power (figure 3.4.2). This is evidence that the CDW order also is far from being suppressed. Indeed, as one approaches the CDW transition the amplitude of the A_{1g} phonon decreases, until it drops to almost 0 above the transition temperature (figure 3.2.1 (f)). Consequently, if we were to significantly disturb the CDW order with the pump power used, we would expect the frequency of the oscillations to at least saturate as the pump power increases.
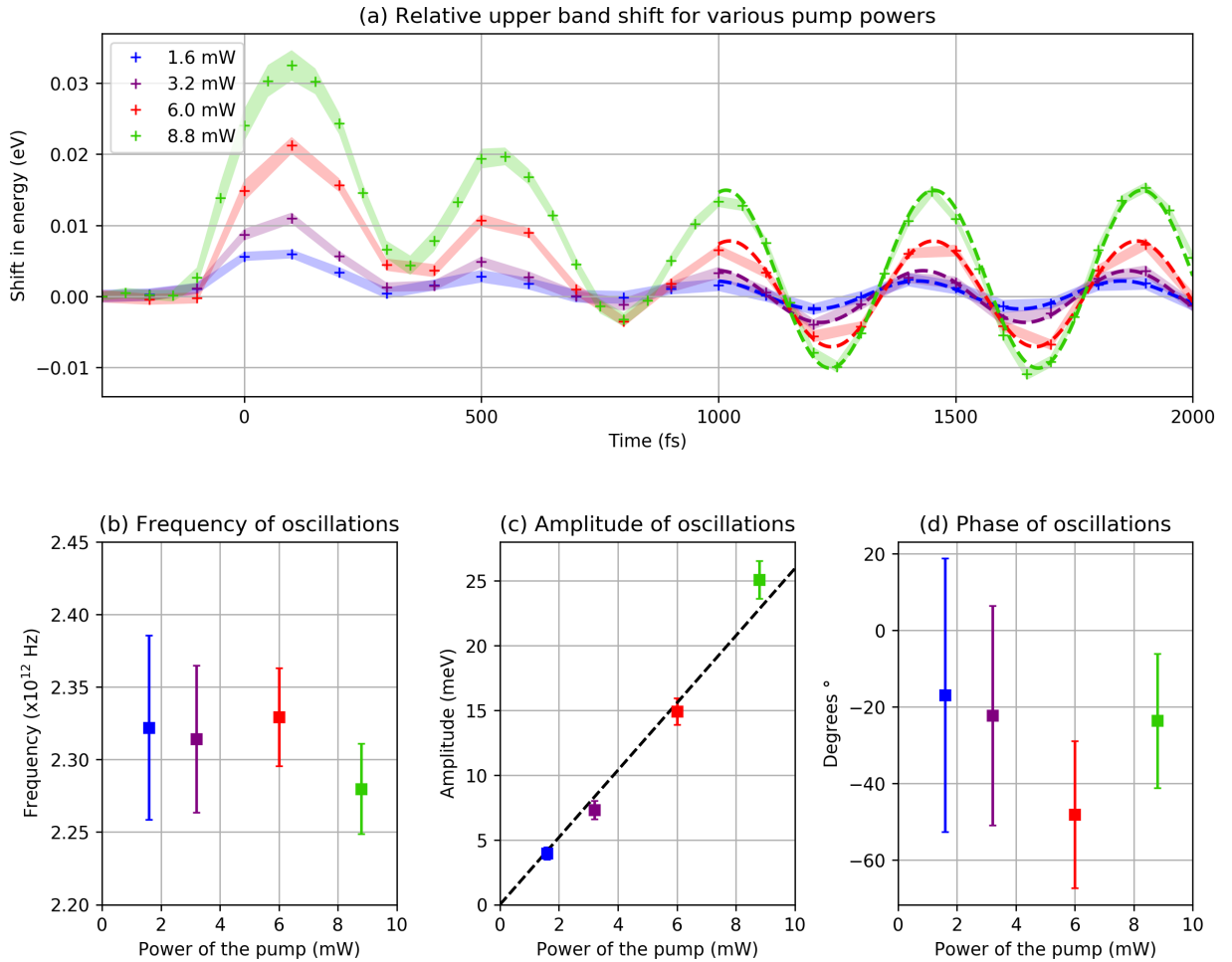
Figure 3.4.2: Systematic study of the oscillations in the upper band shift for all pump powers. Colors from blue to green indicate increasing pump power. (a) The oscillations in the upper band shift are represented in the same way as in figure 3.4.1 (c). (b) Frequency, (c) amplitude, and (d) phase of the oscillations as a function of the pump power. The shaded areas on panel (a) and are the confidence intervals at 95% given by the Voigt function fits. They are taken into account for the fit of the oscillations.

Conclusions

In conclusion, we have investigated the electronic structure and dynamics of two quantum materials using a TR-ARPES experiment. In the topological insulator Bi_2Te_2Se, we have highlighted the contrasted electronic dynamics between the bulk and the surface states. We have also observed in static ARPES measurements the opening of a gap caused by the deposition of magnetic atoms at the surface. For the CDW compound $1T\text{-}TaSe_2$, we have provided strong evidence that the Mott phase is linked to athe in-plane CDW amplitude, since it determines in large part the amount of electron localization between adjacent star-of-David configurations. In addition, neither the Mott phase nor the CDW order are significantly disturbed by the photo excitation. These results highlight the role of the CDW and lattice degrees of freedom in stabilizing the Mott phase of 1T-TaSe2 and further the understanding of the interplay between these coexisting phases.

Acknowledgments

First, I would like to thank Claudia Dallera for proposing this very interesting subject and accepting to supervise this internship.

This work could not have been realized without the help of Hamoon Hedayat, Charles Sayers and Ettore Carpene, who gave me a glimpse of the intricacies of the ARPES technique and data analysis. They managed to contain my naive excitement and taught me to be always more careful with experimental data and its interpretation.

Finally, I would like to thank Andrea, Arianna, Clément, Argyro and all the others for the pleasant atmosphere, the coffee breaks and the pizze on the rooftop.

Bibliography

[1] C. J. Sayers, H. Hedayat, A. Ceraso, F. Museur, M. Cattelan, L. S. Hart, L. S. Farrar, S. Dal Conte, G. Cerullo, C. Dallera, E. Da Como, and E. Carpene, "Coherent phonons and the interplay between charge density wave and Mott phases in 1 T - Ta Se 2," *Physical Review B*, vol. 102, p. 161105, Oct. 2020.

[2] A. Damascelli, "Probing the Electronic Structure of Complex Systems by ARPES," *Physica Scripta*, vol. T109, p. 61, 2004.

[3] F. Boschini, H. Hedayat, C. Dallera, P. Farinello, C. Manzoni, A. Magrez, H. Berger, G. Cerullo, and E. Carpene, "An innovative Yb-based ultrafast deep ultraviolet source for time-resolved photoemission experiments," *Review of Scientific Instruments*, vol. 85, p. 123903, Dec. 2014.

[4] G. Tkachov, *Topological Insulators: The Physics of Spin Helicity in Quantum Transport.* Singapore: Pan Stanford, 2016.

[5] M. Z. Hasan and C. L. Kane, "Topological Insulators," *Reviews of Modern Physics*, vol. 82, pp. 3045–3067, Nov. 2010.

[6] X. Zhu, J. Guo, J. Zhang, and E. W. Plummer, "Misconceptions associated with the origin of charge density waves," *Advances in Physics: X*, vol. 2, pp. 622–640, May 2017.

[7] J.-A. Yan, M. A. D. Cruz, B. Cook, and K. Varga, "Structural, electronic and vibrational properties of few-layer 2H- and 1T-TaSe2," *Scientific Reports*, vol. 5, Dec. 2015.

[8] X. Shi, W. You, Y. Zhang, Z. Tao, P. M. Oppeneer, X. Wu, R. Thomale, K. Rossnagel, M. Bauer, H. Kapteyn, and M. Murnane, "Ultrafast electron calorimetry uncovers a new long-lived metastable state in $1 T$-TaSe$_2$ mediated by mode-selective electron-phonon coupling," *Science Advances*, vol. 5, p. eaav4449, Mar. 2019.

[9] C. Sohrt, A. Stange, M. Bauer, and K. Rossnagel, "How fast can a Peierls–Mott insulator be melted?," *Faraday Discuss.*, vol. 171, pp. 243–257, May 2014.

[10] S. Hüfner, *Photoelectron Spectroscopy: Principles and Applications ; with 28 Tables.* Berlin: Springer, 2003.

[11] F. Boschini, D. Bugini, M. Zonno, M. Michiardi, R. P. Day, E. Razzoli, B. Zwartsenberg, E. H. d. S. Neto, S. dal Conte, S. K. Kushwaha, R. J. Cava, S. Zhdanovich, A. K. Mills, G. Levy, E. Carpene, C. Dallera, C. Giannetti, D. J. Jones, G. Cerullo, and A. Damascelli, "Role of matrix elements in the time-resolved photoemission signal," *arXiv:1810.06571 [cond-mat]*, Oct. 2018.

[12] J. K. Freericks, H. R. Krishnamurthy, and T. Pruschke, "Theoretical Description of Time-Resolved Photoemission Spectroscopy: Application to Pump-Probe Experiments," *Physical Review Letters*, vol. 102, Mar. 2009.

[13] J. K. Asbóth, L. Oroszlány, and A. Pályi, *A Short Course on Topological Insulators*, vol. 919 of *Lecture Notes in Physics.* Cham: Springer International Publishing, 2016.

[14] T. Lancaster and S. Blundell, *Quantum Field Theory for the Gifted Amateur.* Oxford: Oxford University Press, first edition ed., 2014.

[15] M. Fruchart and D. Carpentier, "An Introduction to Topological Insulators," *Comptes Rendus Physique*, vol. 14, pp. 779–815, Nov. 2013.

[16] M. Z. Hasan and J. E. Moore, "Three-Dimensional Topological Insulators," *Annual Review of Condensed Matter Physics*, vol. 2, pp. 55–78, Mar. 2011.

[17] H. Hedayat, D. Bugini, H. Yi, C. Chen, X. Zhou, G. Cerullo, C. Dallera, and E. Carpene, "Surface State Dynamics of Topological Insulators Investigated by Femtosecond Time- and Angle-Resolved Photoemission Spectroscopy," *Applied Sciences*, vol. 8, p. 694, Apr. 2018.

[18] X.-G. Wen, "Zoo of quantum-topological phases of matter," *Reviews of Modern Physics*, vol. 89, p. 041004, Dec. 2017.

[19] M. Hajlaoui, E. Papalazarou, J. Mauchain, G. Lantz, N. Moisan, D. Boschetto, Z. Jiang, I. Miotkowski, Y. P. Chen, A. Taleb-Ibrahimi, L. Perfetti, and M. Marsi, "Ultrafast surface carrier dynamics in the topological insulator Bi2Te3," *Nano Letters*, vol. 12, pp. 3532–3536, July 2012.

[20] L. A. Wray, Y. Xia, S.-Y. Xu, Y. S. Hor, R. J. Cava, A. Bansil, H. Lin, and M. Z. Hasan, "Effects of iron doping on the topological insulator surfaces," *arXiv:1009.6216 [cond-mat, physics:quant-ph]*, Sept. 2010.

[21] Q. Liu, C.-X. Liu, C. Xu, X.-L. Qi, and S.-C. Zhang, "Magnetic impurities on the surface of a topological insulator," *Physical Review Letters*, vol. 102, p. 156603, Apr. 2009.

[22] R. R. Biswas and A. V. Balatsky, "Impurity-induced states on the surface of 3D topological insulators," *Physical Review B*, vol. 81, p. 233405, June 2010.

[23] L. A. Wray, S.-Y. Xu, Y. Xia, D. Hsieh, A. V. Fedorov, Y. S. Hor, R. J. Cava, A. Bansil, H. Lin, and M. Z. Hasan, "A topological insulator surface under strong Coulomb, magnetic and disorder perturbations," *Nature Physics*, vol. 7, pp. 32–37, Jan. 2011.

[24] A. Díaz-Fernández, L. Chico, J. W. González, and F. Domínguez-Adame, "Tuning the Fermi velocity in Dirac materials with an electric field," *Scientific Reports*, vol. 7, Dec. 2017.

[25] N. Ehlen, A. Sanna, B. V. Senkovskiy, L. Petaccia, A. V. Fedorov, G. Profeta, and A. Grüneis, "Direct observation of a surface resonance state and surface band inversion control in black phosphorus," *Physical Review B*, vol. 97, Jan. 2018.

[26] L. Perfetti, P. A. Loukakos, M. Lisowski, U. Bovensiepen, H. Berger, S. Biermann, P. S. Cornaglia, A. Georges, and M. Wolf, "Time Evolution of the Electronic Structure of 1 T - TaS 2 through the Insulator-Metal Transition," *Physical Review Letters*, vol. 97, Aug. 2006.

[27] J. C. Tsang, J. E. Smith, M. W. Shafer, and S. F. Meyer, "Raman spectroscopy of the charge-density-wave state in 1 T - and 2 H - T a Se 2," *Physical Review B*, vol. 16, pp. 4239–4245, Nov. 1977.

[28] A. V. Kuznetsov and C. J. Stanton, "Theory of Coherent Phonon Oscillations in Semiconductors," *Physical Review Letters*, vol. 73, pp. 3243–3246, Dec. 1994.